UNLV University Libraries
University of Nevada, Las Vegas

8-2010

# Wind flow modeling for wind energy analysis of the Nellis Dunes area in Nevada

Upendra Rangegowda
*University of Nevada, Las Vegas*

Follow this and additional works at: https://digitalscholarship.unlv.edu/thesesdissertations

Part of the Atmospheric Sciences Commons, Mechanical Engineering Commons, Oil, Gas, and Energy Commons, and the Sustainability Commons

WIND FLOW MODELING FOR WIND ENERGY ANALYSIS OF THE NELLIS

DUNES AREA IN NEVADA

by

Upendra Rangegowda

Bachelor of Engineering
Visvesvaraya Technological University, India
2003

A thesis submitted in partial fulfillment
of the requirement for the

**Master of Science Degree in Mechanical Engineering**
**Department of Mechanical Engineering**
**Howard R. Hughes College of Engineering**

**Graduate College**
**University of Nevada, Las Vegas**
**August 2010**

We recommend that the thesis prepared under our supervision by

**Upendra Rangegowda**

entitled

**Wind Flow Modeling for Wind Energy Analysis of the Nellis Dunes Area in Nevada**

be accepted in partial fulfillment of the requirements for the degree of

**Master of Science in Mechanical Engineering**

Darrell Pepper, Committee Chair

William Culbreth, Committee Member

Hui Zhao, Committee Member

Laxmi Gewali, Graduate Faculty Representative

Ronald Smith, Ph. D., Vice President for Research and Graduate Studies
and Dean of the Graduate College

**August 2010**

ABSTRACT

**Wind Flow Modeling for Wind Energy Analysis of the Nellis Dunes Area in Nevada**

by

Upendra Rangegowda

Dr Darrell Pepper, Advisor
Professor, Department of Mechanical Engineering
University of Nevada, Las Vegas


A wind energy analysis of the Nellis Dunes area in Nevada was conducted. A DEM file which contains the elevation data was used to generate the surface model and to create a 3-D mesh of the region. Local meteorological tower data collected for a period of one year was used to generate the diagnostic initial wind fields. Upper level wind fields were created using a surface boundary layer technique along with linear interpolation of the tower level wind fields. The vertical components of the velocities were adjusted using the equation of continuity. Mass consistent 3-D wind fields were then calculated using the finite element method. Divergence reduction of the complete wind field was conducted using an iterative procedure.

The statistical analysis of the measured monthly averaged wind data was also performed. The velocity distribution analysis of the measured data was undertaken, and showed a good fit with the Weibull distribution of wind velocity. The wind rose diagrams for all the tower locations were plotted to obtain the monthly averaged wind directions for the entire year.

The wind velocities generated from the mass-consistent wind model were used as input to calculate wind power density maps. Monthly wind power density maps for the entire year were generated. The potential locations for establishing a wind farm is discussed.

TABLE OF CONTENTS

Dedicated to
All My Friends

ACKNOWLEDGEMENTS

LIST OF FIGURES

CHAPTER 1

INTRODUCTION

Wind field prediction and wind power assessment has been a consuming interest for the engineering community for many years. Modeling 3-D wind fields is important for wind energy assessment, weather forecasting, wind turbine sitting and atmospheric dispersion assessments problems. However, it is difficult to generate accurate 3-D wind fields. The main reason is that measurements of atmospheric flows are sparse and generally insufficient to resolve important flow phenomena. A routine approach is to link meteorological data and tower data with a numerical approach. Because of their simplicity and ease of implementation, most of the numerical models used in meteorological simulations use finite-volume and finite-difference techniques. In recent times, these techniques have adopted the use of unstructured meshes, as compared with global transformation techniques used many years ago to account for irregular terrain. For more than 20 years, atmospheric simulations have employed the use of finite-element method due to its abilities to deal with complex geometrical problems with inhomogeneous or variable properties, the use of general purpose algorithms, and significant computational enhancements to reduce storage and speed up solutions (Heinrich and Pepper 1999).

For creating 3D wind fields, mass consistent models have been used for many years and have been found to be very effective in modeling atmospheric dispersion. More recently, such models have been useful in conducting wind energy assessments studies. These modeling techniques are discussed in detail in Sherman (1978), Lange (1978), Goodin et al. (1980), Pepper (1991), Ratto et al. (1994), Finardi et al. (1998), and

Montero and Sanin (2001). Most applications deal with coarse meshes and are unable to utilize mesh refinement where the terrain and/or velocities are complex. Mass consistent models represent a least squares problem in the computational domain (i.e., it minimizes the differences between the observed and adjusted values). These techniques are discussed in detail in Chapter 2.

In this study, a finite element model has been used to create 3-D wind fields utilizing sparse meteorological tower data. Digital elevation map (DEM) data developed by the U.S. Geological Survey (USGS) was used to generate an initial mesh. Meteorological data collected from three tower sites were used to construct the 3D wind fields for the Nellis Dunes Area (see Fig. 1.1 and 1.2).

Wind speed has a cubic relation with power, and is one of the most important factors to consider when assessing power potential of a candidate site. Since wind speed varies by the minute, hour, day, season and year, it is typically averaged over several years to obtain annual speed. Wind is driven by the sun and the seasons, which is the reason wind patterns generally repeat over the period of one year. A wind site is usually categorized from wind speed data averaged over the calendar months. Sometimes the wind data is aggregated over the year to determine the overall "windiness" of various sites. A probability distribution function is then used to describe the wind speed variations over a period of time. In this study, a Weibull Probability Distribution has been used to describe the variation of wind speed (Patel, 2006).

The wind data for this study was collected for the Nellis Dunes area northeast of Nevada (as shown in Fig. 1.1 and 1.2) for the time period of January 1, 2008 to February 1, 2009. Four meteorological towers were erected in the Nellis Dunes area. The locations

of the towers are shown in Fig. 1.2 and Table 1. Wind speeds and directions were recorded for every 10 min over the period from October 18th, 2008 to February 1st, 2009 using Symphonie data loggers (Symphonie User's Manual, 2006. see Figure. 1.3). Also, monthly averaged data was recorded for the period from January 1st, 2008 to October 17th, 2008.



Figure 1.1 Location of Nellis dunes area (Courtesy: Google Maps)

Figure 1.2 Locations for the four meteorological towers (Courtesy: Google Maps)
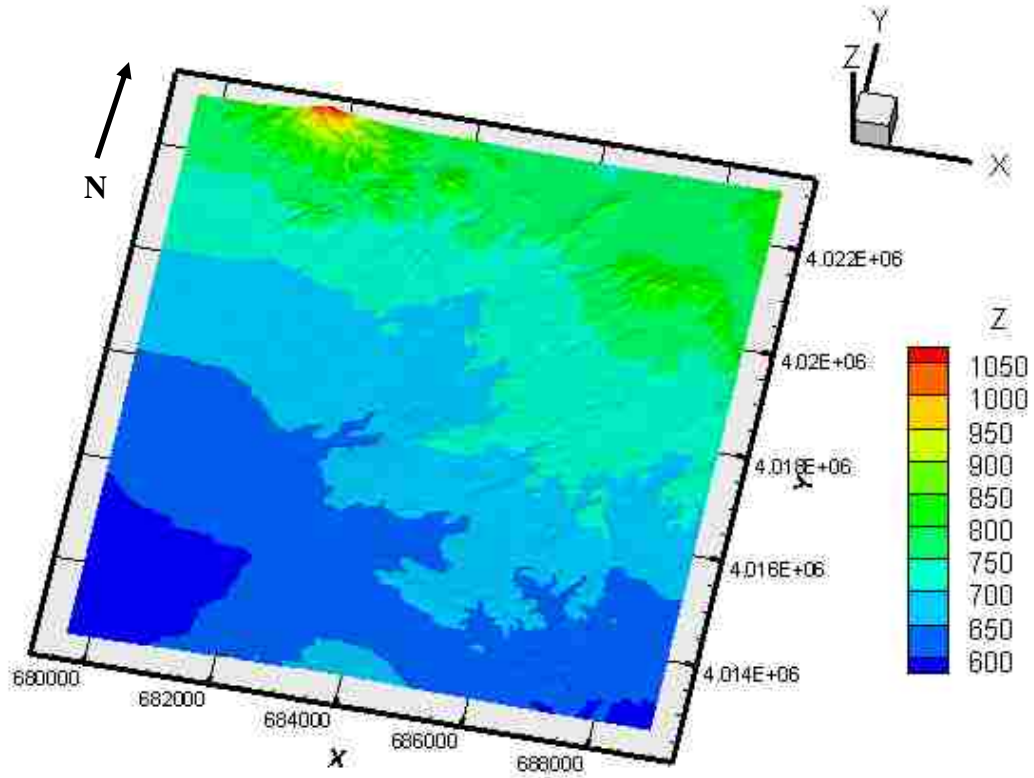
Figure 1.3  Topography of the Nellis dunes Area

Table 1.1 Tower Descriptions

| Site No. | Elevation (m) | Latitude, Longitude |
|----------|---------------|---------------------|
| Tower 1 | 20 | N 3617717, W 11455446 |
| Tower 2 | 20 | N 3616761, W 11458210 |
| Tower 3 | 20 | N 3616162, W 11457560 |
| Tower 4 | 10 | N 3618457, W 11456214 |

Figure 1.4 Towers to measure the wind data

Figure 1.5 Symphonie data logger

CHAPTER 2

NUMERICAL WIND FLOW PREDICTION

## 2.1 Governing Equations of Fluid Dynamics

The governing equations of motion which describe the atmospheric flows are the conservation of mass, momentum, energy and species transport. Based on Pielke (1984), the governing equations for a three-dimensional atmospheric flow are:

Conservation of Mass:

$$\frac{\partial p}{\partial t} + \frac{\partial(\rho u)}{\partial x} + \frac{\partial(\rho v)}{\partial y} + \frac{\partial(\rho w)}{\partial z} = 0 \qquad 2.1$$

Conservation of Momentum:

x-direction:

$$\frac{\partial(\rho u)}{\partial t} + \frac{\partial(\rho u^2)}{\partial x} + \frac{\partial(\rho uv)}{\partial y} + \frac{\partial(\rho uw)}{\partial z} = \frac{\partial}{\partial x}\left(k_h \frac{\partial u}{\partial x}\right) + \frac{\partial}{\partial y}\left(k_h \frac{\partial u}{\partial y}\right) +$$
$$\frac{\partial}{\partial z}\left(k_z \frac{\partial u}{\partial z}\right) + 2v\omega\sin\psi - 2w\omega\cos\psi - \frac{\partial p}{\partial x} \qquad 2.2$$

y-direction:

$$\frac{\partial(\rho v)}{\partial t} + \frac{\partial(\rho uv)}{\partial x} + \frac{\partial(\rho v^2)}{\partial y} + \frac{\partial(\rho vw)}{\partial z} = \frac{\partial}{\partial x}\left(k_h \frac{\partial v}{\partial x}\right) + \frac{\partial}{\partial y}\left(k_h \frac{\partial v}{\partial y}\right) +$$
$$\frac{\partial}{\partial z}\left(k_z \frac{\partial v}{\partial z}\right) - 2u\omega\sin\psi - \frac{\partial p}{\partial y} \qquad 2.3$$

z-direction:

$$\frac{\partial(\rho w)}{\partial t} + \frac{\partial(\rho uw)}{\partial x} + \frac{\partial(\rho vw)}{\partial y} + \frac{\partial(\rho w^2)}{\partial z} = \frac{\partial}{\partial x}\left(k_h \frac{\partial w}{\partial x}\right) + \frac{\partial}{\partial y}\left(k_h \frac{\partial w}{\partial y}\right) +$$
$$\frac{\partial}{\partial z}\left(k_z \frac{\partial w}{\partial z}\right) - g - \frac{\partial p}{\partial z} \qquad 2.4$$

Conservation of Energy:

$$\frac{\partial \theta}{\partial t} + \frac{\partial (u\theta)}{\partial x} + \frac{\partial (v\theta)}{\partial y} + \frac{\partial (w\theta)}{\partial z} = \frac{\partial}{\partial x}\left(k_h \frac{\partial \theta}{\partial x}\right) + \frac{\partial}{\partial y}\left(k_h \frac{\partial \theta}{\partial y}\right) +$$
$$\frac{\partial}{\partial z}\left(k_z^\theta \frac{\partial \theta}{\partial z}\right) + \left(\frac{\partial \theta}{\partial t}\right)_{rad}$$

2.5

Specific Humidity:

$$\frac{\partial q}{\partial t} + \frac{\partial (uq)}{\partial x} + \frac{\partial (vq)}{\partial y} + \frac{\partial (wq)}{\partial z} = \frac{\partial}{\partial z}\left(k_z^q \frac{\partial q}{\partial z}\right)$$

2.6

Species Transport:

$$\frac{\partial C_m}{\partial t} + \frac{\partial (uC_m)}{\partial x} + \frac{\partial (vC_m)}{\partial y} + \frac{\partial (wC_m)}{\partial z} = \frac{\partial}{\partial x}\left(k_h \frac{\partial C_m}{\partial x}\right) + \frac{\partial}{\partial y}\left(k_h \frac{\partial C_m}{\partial y}\right) +$$
$$\frac{\partial}{\partial z}\left(k_z \frac{\partial C_m}{\partial z}\right) + S_{C_m}$$

2.7

where u, v, w are the east-west (x), north-south (y), and vertical (z) components of velocity, respectively; $\omega$ is the angular velocity of the earth; $\psi$ is the latitude; $\theta$ is the potential temperature; q is the specific humidity; $C_m$ is the species concentration; g is the acceleration of gravity; $\left(\frac{\partial \theta}{\partial t}\right)_{rad}$ is the radiative heating/cooling of the atmosphere; $S_{C_m}$ is the source/sink term which includes changes of state, chemical transformations, precipitation, and sedimentation; $k_h$ is the horizontal diffusion coefficient; and $k_z$ is the vertical diffusivity.

The potential temperature is defined as:

$$\theta = T_V (1000/p)^{R_d/C_p}$$

2.8

where the unit of pressure $p$ is in mb, $T_v$ is the virtual temperature , $C_p$ is the specific heat at constant pressure, and $R_d$ is the universal gas constant.

The ideal gas law is written as:

$$p = \rho R_d T_V$$

2.9

where the density $\rho$ is defined as the inverse of the specific volume. The virtual temperature is defined as:

$$T_v = T(1 + 0.61q)$$

2.10

The pressure can be obtained from the hydrostatic assumption (normally this is used in many atmospheric models) or from solution of the "discrete" momentum equations and a simple poisson equation. The velocity components are adjusted by using a potential function which is solved from the Poisson equation (Pepper and Brueckner, 1992).

The modeling of turbulence and resulting forms of closure are quite varied; the gradient diffusion approach is typically used (Pepper and Brueckner, 1992). Using the relation proposed by Smagorinsky et al. (1965), the horizontal mixing is approximated and Anthes and Warner (1978) later used this. For example, the horizontal mixing intensity is related to the wind shear strength, e.g.,

$$k_h = \frac{1}{2} k_0^2 h_e^2 \left[ \left( \frac{\partial u}{\partial x} - \frac{\partial v}{\partial y} \right)^2 + \left( \frac{\partial v}{\partial x} + \frac{\partial u}{\partial y} \right)^2 \right]^{\frac{1}{2}}$$

2.11

where $k_0$ is the von Karman's constant and $h_e$ is the average element length.

In the surface layer the vertical exchange coefficients of momentum, heat, and moisture are given by the relations:

$$k_z = \frac{k_0 u^* z}{\phi_m(\zeta)}$$

2.12

and

10

$$k_z^\theta = k_z^q = \frac{k_0 u^* z}{\phi_H(\zeta)}$$ 

<span style="float:right">2.13</span>

where $u^*$ is the friction velocity; $\phi_m$ is the nondimensional wind profile; $\phi_H$ is the surface layer mean vertical temperature profile; and $\zeta = z/L$, where L is Monin-Obukhov length. The expression for the nondimensional wind and potential temperature profiles according to Businger et al. (1971) are:

$$\phi_m = \begin{cases} (1-15\zeta)^{-1/4} & \zeta \leq 0 \\ (1-4.7\zeta) & \zeta > 0 \end{cases}$$

<span style="float:right">2.14</span>

$$\phi_H = \begin{cases} 0.74(1-9\zeta)^{-1/2} & \zeta \leq 0 \\ (0.74+4.7\zeta) & \zeta > 0 \end{cases}$$

<span style="float:right">2.15</span>

The exchange coefficients above the surface layer are defined according to McNider and Pielke (1981). The thermodynamical stability of the surface controls the coefficients. The local exchange coefficients suggested by Blackadar (1979) are used when this layer is stable. The profile function of O'Brien (1970) is used when the surface layer is stable.


## 2.2 The Finite Element Method

Though the derivations of most of the fluid flow governing equations are not unduly difficult, it is a formidable task to obtain the solutions to those equations by exact methods. This is the case where the approximate methods of analysis provide the alternative means of finding the solutions. The finite difference method, the variational method, and the finite element method are the most frequently used methods to obtain the approximate solutions.

Similar to the finite difference scheme, in the finite element method the problem defined in the geometrical space (domain) is subdivided in to a finite number of small regions (mesh). In finite-difference and finite-volume methods the mesh consisted of rows and columns of orthogonal lines (this requirement can be handled through coordinate transformations or unstructured mesh generators); but in the finite-element method each subdivision is unique and it does not need to be orthogonal (Pepper and Heinrich 2006). Triangles and quadrilaterals are commonly used in two dimensions and tetrahedrons and hexahedrons are used in three dimensions. For example, an unknown variable (temperature, velocity, etc.) is approximated using the known functions (called shape functions) over each discretized element in the finite-element method. Based on the geometrical locations (nodes) used to define the finite element shape, these functions can be linear or higher-order polynomial expansions. In finite-element procedures, the governing equations are integrated over each finite-element and the contributions are summed (assembled) over the entire problem domain. In the finite-difference method, Taylor series approximations are used to create difference discretizations; in the finite volume method, a simple integration is performed over each volume to conserve mass. A set of finite linear equations are obtained in terms of a set of unknown parameters over the elements. Using linear algebra techniques, solutions can be obtained which stem from sparse matrices (which can be solved efficiently).

The basis for the finite element method lies in the Galerkin method of weighted residuals and by which it minimizes the error throughout the computational domain. The Galerkin method is guaranteed to yield a compatible approximation to the governing equations and also is simple to use. In the Galerkin method, the dependent variable is

expressed by means of a finite series approximation in which the "shape" of the solution is assumed known, and depends on a finite number of parameters to be determined. The approximation generates a residual function when replaced in the governing equation, which is multiplied by weighting functions and is required to be orthogonal to the weighting functions in the integrated sense, i.e.,

$$\int W(x)R(\Phi, x)d(x) = 0 \qquad\qquad 2.16$$

where $\Phi$ is the unknown variable, $R(\Phi, x)$ is the residual error function ( the function obtained when the approximation to the exact solution of $\Phi$ is replaced in the differential equation), x is the length coordinate, and W(x) is the weight. To determine the unknown parameter $\Phi$ , a set of linear algebraic equations can be generated from these expressions, and hence an approximation to the solution (Pepper and Heinrich, 1992).


## 2.3 Numerical Modeling

A mass-consistent diagnostic model can be derived from the continuity equation utilizing actual wind data. "Diagnostic" is the term which was used by Pielke (1984) to discuss different mesoscale meteorological models. Sherman (1978) undertook the early research work on the mass-consistent model that was later applied by Pepper using an FEM approach (1991). The main idea of the mass-consistent model is to reduce the difference between the simulation results and the measured meteorological data. This uses the weighted averaging around the (usually) sparse data points to fill in the values to all the nodes of the domain and to match the simulation values with the meteorological values.

Using interpolation a surface wind field can be constructed over an initial mesh of a region using the measured data and inverse squared weighting ($1/r^2$, where $r$ is the radial distance between the grid points and the tower locations). A fixed radius R, is specified and beyond that radius the effect of a tower's value is no longer felt (Goodin et al. 1979; Kitada et al. 1983; Pepper 1991). R is evaluated with two values: R=L/N and R=L, where L is the length of the horizontal region and N is the number of observations. In the evaluation of the field data the use of the former R = L/N gives better results (Goodin et al. 1979; Kitada et al.1983).

Upper layer velocity can be calculated from the horizontal level velocity, i.e., the velocity at an upper layer grid point is calculated from the velocity at the grid point that has the same horizontal level as the tower layer. Using log-linear interpolation the top-layer velocity can be calculated.

Estimation of the vertical wind velocity is one of the more difficult problems associated with wind modeling studies. In diagnostic and prognostic problems, the vertical velocity is an integral component. Using the horizontal wind observations and accounting for divergence correction, the vertical velocities are calculated at all grid points from the continuity equation, that is,

$$w = -\int_0^z \left( \frac{\partial u}{\partial x} + \frac{\partial v}{\partial y} \right) dz, \qquad\qquad 2.17$$

where u, v and w are velocities in the x, y and z directions respectively.

## 2.4 Mass-consistent FEM

Since its inception in the mid 1950s, the finite-element method is a popular numerical technique that has been used by engineers and scientists to solve many structural problems. The application of finite-element methods to other fields, particularly to the fluid flow, started to occur around the late 1970s (Zienkiewicz and Zhu 1987), from then it has been continued to mature over the years.

Finite-difference and finite-volume methods were commonly used in the past for fluid modeling. In its capabilities to deal with the complex geometries, the finite-element method is more attractive in comparison with the finite-difference methods. The discretization of the variables and the gradient terms are based upon the Taylor series approximation and nodal molecules in the finite-difference method (this is usually three point approximations yielding second-order spatial accuracy in each direction). Since the finite-element method uses basis functions to approximate the spatial distances (via elements instead of node point intervals), it allows one to capitalize on a family of interpolations that can yield much higher spatial accuracies.

In the finite-element method, the computational accuracy can be increased by two ways- either by using a fine mesh (refinement) or by applying higher-order approximation (enrichment). When doing atmospheric calculations it is typically impractical to use a uniform fine mesh or higher order approximations over the entire domain; this is because atmospheric calculations usually require huge computational resources. This is where local adaptation can be very useful, since the adaptive finite-element method allows one to use local refinement (h-adaptation) or local enrichment (p-

adaptation), thereby significantly reducing the computational time and storage when compared to the globally refined or enriched meshes ( see Wang and Pepper 2007a, b).

Lange (1978) at Lawrence Livermore National Laboratory was the first to use a 3-D mass consistent model to generate wind fields for the Atmospheric Diffusion Particle-in-Cell (ADPIC) pollutant transport model. Dickerson (1978) and Sherman (1978) constructed a mass-consistent model in their work. Their technique was based on an objective analysis approach using a Sasaki variational technique (Sasaki 1958). Matur and Peters (1990) and Pepper (1991) applied this technique for air pollution modeling. Pepper (1991) applied this method using FEM to predict meso-scale wind fields over Vanderberg Air Force Base. Genetic algorithms for improved parameter estimation with local tetrahedral mesh refinement in a wind model were developed by Montero et al. (2005). Ratto et al. (1994) discusses the selection of parameters and computational methods implemented by different mass consistent models. Because of its simplicity and ease of implementation with adaptivity we have selected this approach in lieu of others. Warner et al. (1983) describes the use of observed winds versus the predicted winds employing a 3D dynamic model to predict the medium range atmospheric transport, along with shortcomings in accuracies attributed to each technique.

In this procedure, an Euler-Lagrange method is used in an integral function that minimizes the variance of the difference between the observed and analyzed variables (Sasaki 1958). This function is written as

$$E(u,v,w,\lambda) = \int_{\Omega} \left[ \alpha_1^2 (u-u_0)^2 + \alpha_1^2 (v-v_0)^2 + \alpha_2^2 (w-w_0)^2 + \lambda \left( \frac{\partial u}{\partial x} + \frac{\partial v}{\partial y} + \frac{\partial w}{\partial z} \right) \right] d\Omega,$$

2.18

16

where, $u_0, v_0$ *and* $w_0$ are the values of the observed velocities in the *x, y* and *z* direction respectively, and $\Omega$ is the physical domain ($d\Omega \equiv dxdydz$), and $\alpha_i$ are the Gauss precision moduli, where $\alpha_i^2 = 1/2\sigma_i^2$ ($\sigma_i$ are the observation tower errors and/or deviations of the observed field from the desired adjusted field). Since apparent distinctions exist between the horizontal and vertical directions but not between x and y coordinates, the Gauss precision moduli are assumed identical for the horizontal directions (Sherman 1978). For determining the nondivergence wind field over irregular terrain these moduli are very important. Sherman (1978) suggested that the $(\alpha_1/\alpha_2)^2$ should be proportional to the magnitude of the expected $(w/u)^2$. Using studies from Kitada et al. (1983) and from the above relation, the 3D wind fields tested for the minimum residual divergence occurred at about $(\alpha_1/\alpha_2)^2 = 0.01$. We have taken the values of $\alpha_1$ and $\alpha_2$ as 0.01 and 0.1 respectively in this study.

The Euler-Lagrange equations, the solutions of which will minimize the equation (2.18) are as follows (Sherman 1978; Kitada et al. 1983; Pepper 1991; Ratto et al. 1994)

$$u = u_0 + \frac{1}{2\alpha_1^2}\frac{\partial\lambda}{\partial x}, \qquad\qquad 2.19$$

$$v = v_0 + \frac{1}{2\alpha_1^2}\frac{\partial\lambda}{\partial y}, \qquad\qquad 2.20$$

and $\qquad\qquad w = w_0 + \frac{1}{2\alpha_2^2}\frac{\partial\lambda}{\partial z}, \qquad\qquad 2.21$

where $\lambda$ = Lagrange multiplier.

Since the velocities are low in this case we can assume the air density as constant in the computational domain; however we can take a variable density to account for the vertical temperature variation if warranted (see Sherman 1978). Now, substituting the equations (2.19) – (2.21) into the continuity equation,

$$\frac{\partial u}{\partial x} + \frac{\partial v}{\partial y} + \frac{\partial w}{\partial z} = 0 \qquad\qquad 2.22$$

a Poisson equation for $\lambda$ (x, y, z) can be obtained of the form,

$$\frac{\partial^2 \lambda}{\partial x^2} + \frac{\partial^2 \lambda}{\partial y^2} + \left(\frac{\alpha_1}{\alpha_2}\right)^2 \frac{\partial^2 \lambda}{\partial z^2} = -2\alpha_1^2\left(\frac{\partial u_0}{\partial x} + \frac{\partial v_0}{\partial y} \frac{\partial w_0}{\partial z}\right). \qquad 2.23$$

The $\alpha_1 / \alpha_2$ ratio will allow one to adjust between the horizontal or vertical influential preference.

After applying the Galerkin method of weighted residuals, the integral form of equation (2.23) can be written as

$$\int_\Omega N_i\left[-\frac{\partial^2 \lambda}{\partial x^2} - \frac{\partial^2 \lambda}{\partial y^2} - \left(\frac{\alpha_1^2}{\alpha_2^2}\right)\frac{\partial^2 \lambda}{\partial z^2} - 2\alpha_1^2\left(\frac{\partial u_0}{\partial x} + \frac{\partial v_0}{\partial y} + \frac{\partial w_0}{\partial z}\right)\right]d\Omega = 0, \qquad 2.24$$

where $N_i$ is the shape function. The matrix equivalent for the above equation can be written as

$$\mathbf{K}\,\lambda = \mathbf{f}, \qquad\qquad 2.25$$

where $\mathbf{K}$ is the stiffness matrix, which is

18

$$\mathbf{K} = \int_{\Omega} \left( \frac{\partial N_i}{\partial x} \frac{\partial N_j}{\partial x} + \frac{\partial N_i}{\partial y} \frac{\partial N_j}{\partial y} + \frac{\alpha_1^2}{\alpha_2^2} \frac{\partial N_i}{\partial z} \frac{\partial N_i}{\partial z} \right) d\Omega \qquad 2.26$$

Note that $\mathbf{f}$ is the load vector (or the right-hand side of the equation), which is,

$$\mathbf{f} = 2\alpha_1^2 \int_{\Omega} N_i \left( \frac{\partial u_0}{\partial x} + \frac{\partial v_0}{\partial y} + \frac{\partial w_0}{\partial z} \right) d\Omega \qquad 2.27$$

The use of this particular technique was within a factor of 2 around 50% of the time and within an order of magnitude about 90% of the time (see Sherman (1978) and Dickerson (1978)). But, the mesh routinely used at the time of their results was a coarse mesh. With the application of adaptation, one can get a more detailed visualization and help in assessing the dynamics of the flow properly.

## 2.5 Atmospheric Boundary Layer Concept

At high Reynolds numbers the influence of viscosity is confined to a very thin layer in the immediate neighborhood of the solid surface, for the fluid flow where the measured pressure distribution nearly agrees to the perfect fluid theory. The velocity of the fluid increases from zero at the surface (no slip) to its full value which corresponds to the external frictionless flow in this layer. This thin layer under consideration is called the *boundary layer.* Similar to boundary layers found in engineering fluid mechanics problems, an atmospheric boundary layer exists for the atmospheric motion.

The velocity distribution in such a boundary layer along a surface is shown in Figure 2.1 (the dimensions across it are considerably exaggerated). The velocity distribution is uniform in front of the leading edge of the surface. The thickness δ, of the retarded layer

increases continuously with increasing distance from the leading edge in the downstream direction, as the increasing quantities of the fluid become affected.
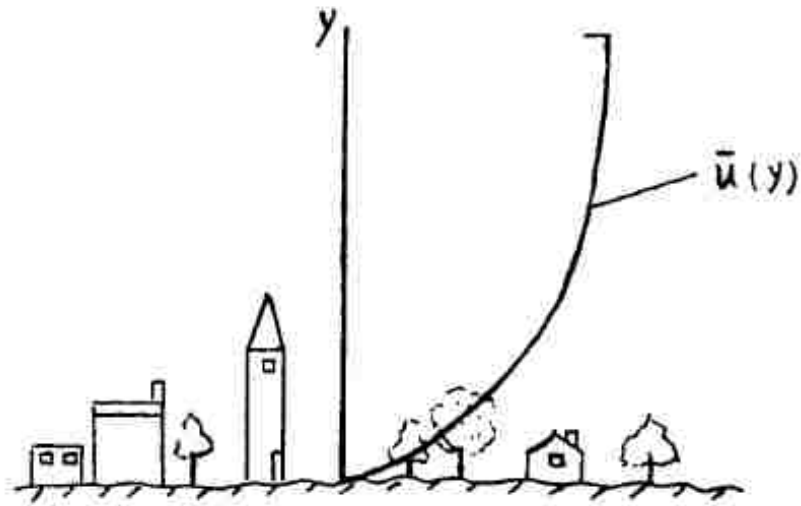


Figure 2.1 Neutrally stratified boundary layer over uniform terrain

For small scale flows, the thickness of the boundary layer which has not separated can be estimated in the following way (Schlichting, 1979).

$$\delta = 5\sqrt{\frac{vl}{U}}$$ 2.28

Referring to the length of the surface $l$ , the dimensionless boundary-layer thickness is:

$$\frac{\delta}{l} = 5\sqrt{\frac{v}{Ul}} = \frac{5}{\sqrt{R_l}}$$ 2.29

where $R_l$ is the Reynolds number related to the length of the surface, $l$, $\nu$ is the kinematic viscosity, and U is the velocity outside the boundary layer.

The concept is the same for the atmospheric boundary layer. The atmospheric boundary layer is quite thin over the surface of smooth water or ice, and much thicker over hilly, tree covered, or urban terrains with large buildings. The boundary layer typically extends upward about 200 to 500 meters (650 to 1,640 feet), but it can also be very thin as 50 meters (164 feet) or as deep as 2 km (6,563 feet). The thickness of the boundary layer also varies with the latitude.

CHAPTER 3

ANALYSIS OF 3D WIND FIELDS

The full solution of the Navier-Stokes equations is not feasible to create in a production code for predicting 3-D wind fields. The use of interpolation of sparse data measurements is done first, followed by the use of an objective analysis to adjust the wind vectors at each grid point within the computational domain. This is the simplest approach for generating a gridded wind field.

In early times, point-iterative methods and/or variational calculus with Lagrangian multipliers to adjust velocities was used to reduce divergence (Pepper and Kern, 1976; Sherman, 1978; and Pielke, 1984). These techniques allowed quick estimates of the wind flow field to be generated and were also relatively simple to use. However, the velocities at the domain boundaries can force the nature of the interior flow solution (Pepper and Brueckner, 1992); Likewise, the empirically chosen constants have control over the flow field. Surface topography was not accurately used in most of the early work and some of the techniques did not employ terrain-following coordinate systems. The basic grid size, vertical extent and the region boundaries for the Nellis Dunes area are first selected. Vertical height (generally of the mixing layer) and the terrain irregularity affect such cell sizes. Once the mesh is generated over the terrain, the measured velocities at the tower level are interpolated to obtain initial velocities at each computational node point. The interpolated velocity field is then adjusted using the finite element method to minimize the divergence of the flow field.

## 3.1 Surface Mesh Generation

The topographical elevation data obtained from the U.S. Geological Survey (USGS) in the form of Digital Elevation Map (DEM) was used to generate the surface topography. The Nellis Dunes area is located in southern Nevada (North of Las Vegas). The Nellis Dunes are located within the area defined by longitude of W114544446 to W11459210 and latitude N3626162 to N3628457. The elevation data was changed to $x -$ $y$ coordinates, where $x -$ direction is East $-$ West and $y -$ direction is North $-$ South. The surface topography was generated using a mesh consisting of 31 x 35 elevation data. The three-dimensional terrain plot of the Nellis Dunes is shown in Figure 3.1. The horizontal surface grid used a 300 m x300 m spacing between the nodes in x and y directions.

Out of the four towers were set up at the Nellis dunes, data from only three of the towers was used in the simulation, since the fourth tower (10m tower) was vandalized and the data was not available for the whole year. The partially available data from the fourth tower was used to validate the simulated values with the recorded values. Since these three towers were not located at the orthogonal mesh points, the surface mesh was altered to fix the three towers at the nodal points.
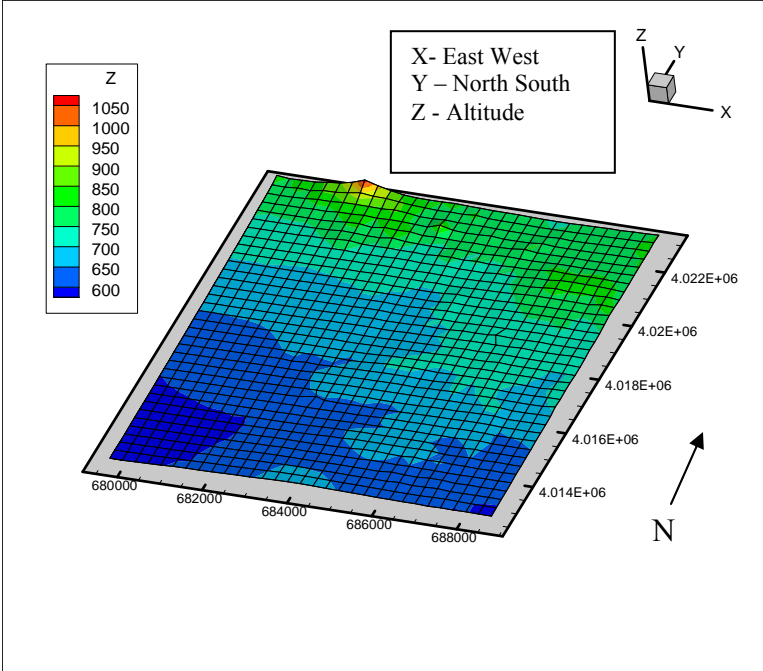
Figure 3.1  A 3-D Terrain of the Nellis dunes area
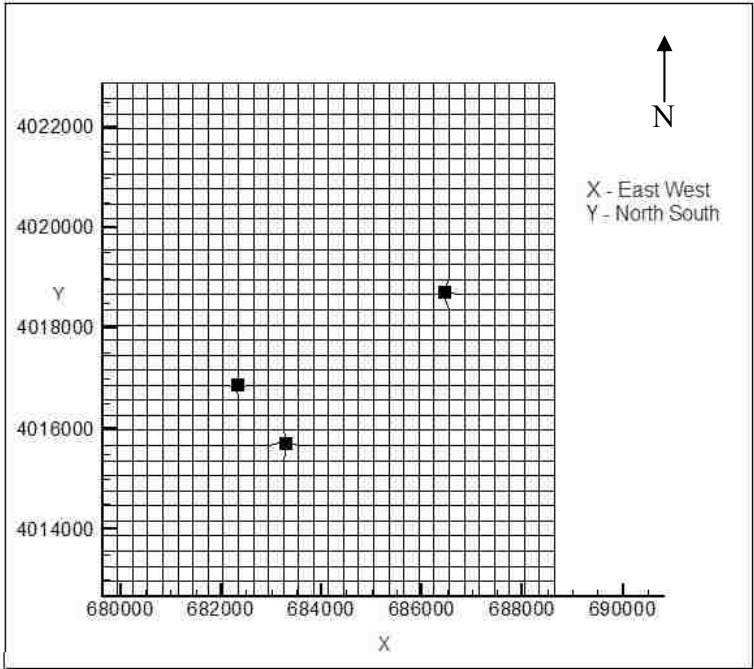


Figure 3.2  Non-orthogonal mesh with the three towers as grid points for the Nellis dunes

## 3.2 Three Dimensional Mesh Generation

A three dimensional mesh for six separate horizontal layers was generated above the ground. A Total of seven layers (including the surface layer) were used to establish the 3-D hexahedral mesh over the region. Layer 1 is the surface layer. Layer 2 is the height at 10 m above the surface - one of the towers had a height of 10 m. Layer 3 is 20 m above the surface layer and three of the other towers were at 20 m heights. Layer 4 is 50 m above the surface layer. Layer 5 is 100 m above, layer 6 is 500 m and layer 7 is 1000 m above the surface layer. A FORTRAN code was applied to generate the 3-D mesh, nodal points and element connectivity. The surface mesh data file was used to initialize the mesh generation scheme. A total of 7595 nodes and 6120 elements were generated for the three dimensional mesh of the Nellis Dunes region (see Figure 3.3). A 2-D cross sectional view of the Nellis Dunes area is shown in Figure 3.4.
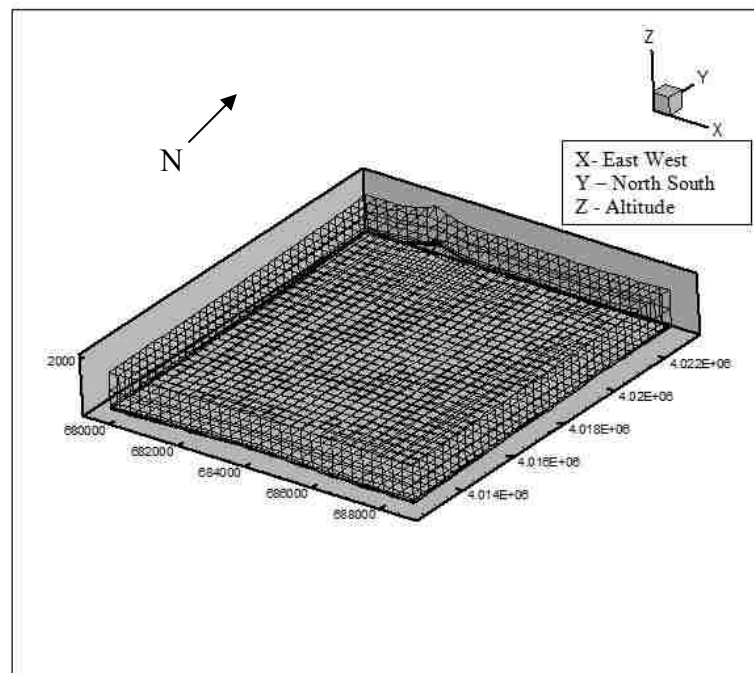


Figure 3.3  3-D mesh of the Nellis dunes area
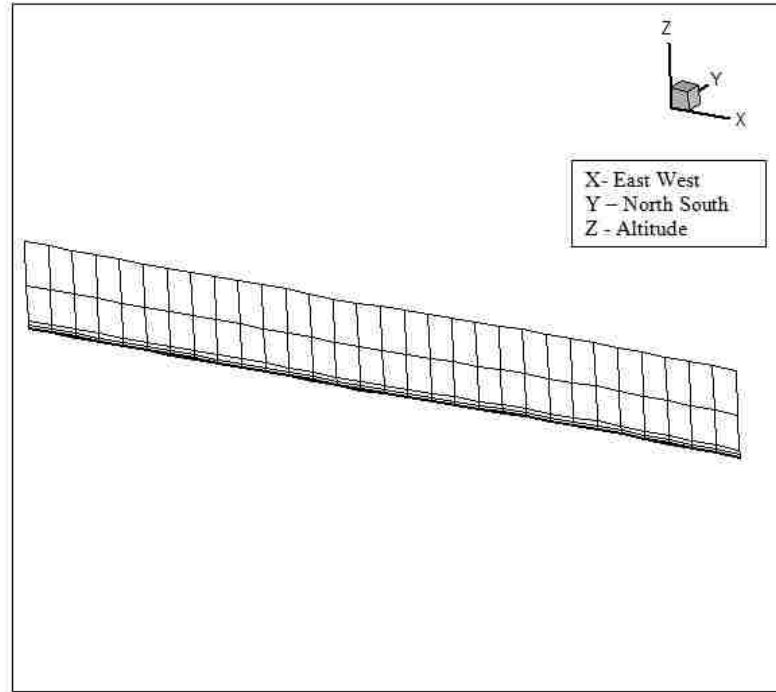
Figure 3.4  2-D Cross sectional view of the mesh for Nellis dunes area

## 3.3 Initial Wind Field Generation

The initial wind field is generated using the measured meteorological data from the three towers (converted into $u$ and $v$ components) by interpolation over the initial mesh using inverse-distance squared weighting (Pepper and Kern, 1976). A fixed radius of influence (R) is specified, which indicates that the influence of a station's value is no longer felt beyond that R (Pepper and Brueckner, 1992). By utilizing simple differences to initially specify velocity components within the computational domain, the gross terrain features (mountain ranges, etc.) can be easily accounted.

## 3.4 Tower Data Formulation

The wind data collected from the three towers were used for interpolation over the mesh (see Figure 3.5). A 10 minute average meteorological data was recorded for the period from October 18th, 2008 to February 1st, 2009 and monthly averaged data was recorded for the period from January 1st, 2008 to October 17th, 2008. The 10 minute average data was used to produce simulation results for those periods consisting of 10 minute averaged values. The data for the 10 minute average was recorded in the polar coordinate system with wind speed in m/s and direction in degrees counting clockwise (where 0/360 degree corresponds to North and 90 degree corresponds to East). The data was converted to $u$ and v cartesian components. A FORTRAN code was used to read the data from all four towers. A top view of the tower locations with the wind vectors within the Nellis Dunes area is shown in Figure 3.6.
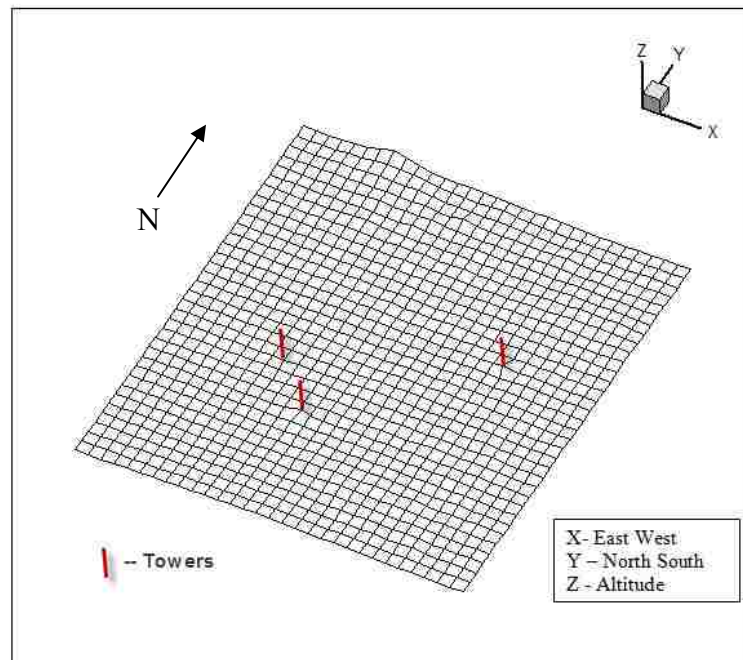


Figure 3. 5 The tower locations in the Nellis dunes area
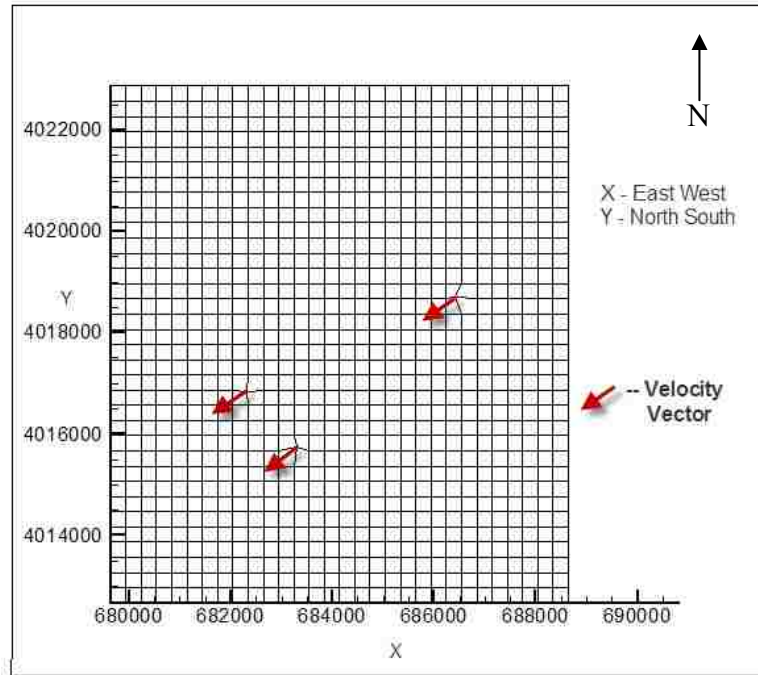
Figure 3. 6 A top view of the tower wind vectors in Nellis dunes area

## 3.5 Tower Layer Velocity Generation

After reading the tower data, an inverse weighting was performed around each tower to obtain tower layer velocities (Goodin, et al, 1979). The velocities at the grid points near the tower were calculated using the measured wind velocities from the tower. The velocity from the tower decays as $1/r^2$ with distance from the tower. Therefore,

$$W(r) = \begin{cases} 1/r^2 & r \leq R \\ 0 & r > R \end{cases} \qquad \text{3.1}$$

Then the velocities at the grid points are given by,

$$u(x, y) = W(r)u_{tower}(x_t, y_t) \qquad \text{3.2a}$$

$$v(x, y) = W(r)v_{tower}(x_t, y_t)$$
3.2b

where $r = \sqrt{(x - x_t)^2 + (y - y_t)^2}$, which is the radial distance between the node (x, y)

and the tower $(x_t, y_t)$. For r > R, u(x,y) = 0, v(x,y) = 0

where R is the radius of influence, (R=4500 meters), and $(x_t, y_t)$ is the closest tower

location from the node (x, y). The tower velocities are labeled $u_t$ in the x-direction and $v_t$

in the y-direction.

## 3.6 Tower Layer Divergence Reduction

After establishing the tower layer wind velocities using the measured data from the

wind towers, the interpolated values at all the nodes of the tower layer must be checked

to minimize the divergence, i.e., try to ensure that $\nabla \bullet \vec{V} \cong 0$. The tower layer values are

smoothed using a slightly modified version of the simple-point filter. The new value at

any given point will be the average of the value at the point and the values at the four

nearest points. The smoothing equations are:

$$u_{i,j}^{n+1} = 0.2(u_{i,j}^n + u_{i+1,j}^n + u_{i-1,j}^n + u_{i,j+1}^n + u_{i,j-1}^n)(1 - \alpha_k) + \alpha_k u_{i,j}^n$$
3.3

$$v_{i,j}^{n+1} = 0.2(v_{i,j}^n + v_{i+1,j}^n + v_{i-1,j}^n + v_{i,j+1}^n + v_{i,j-1}^n)(1 - \alpha_k) + \alpha_k v_{i,j}^n$$
3.4

where $\alpha_k$ is a parameter which is used to keep the measured velocity at station k fixed

($\alpha_k = 1$) or to keep only some of its original influence ($\alpha_k < 1$) and is zero at all non-

measuring station points. $u_{i,j}$ and $v_{i,j}$ are the horizontal velocities of the tower layer. In the

finite element method, $u_{i,j}$ and $v_{i,j}$ cannot be used since the mesh is unstructured.

29

Therefore u(i) and v(i) are used instead, where i is the node number, as defined by its nodal connectivity within an element. Now equations 3.3 and 3.4 can be written as:

$$u(i)^{n+1} = 0.2(u(i)^n + u(i+1)^n + u(i-1)^n + u(i+ncolum)^n +$$
$$u(i-ncolum)^n)(1-\alpha_k) + \alpha_k u(i)^n$$

3.5

$$v(i)^{n+1} = 0.2(v(i)^n + v(i+1)^n + v(i-1)^n + v(i+ncolum)^n +$$
$$v(i-ncolum)^n)(1-\alpha_k) + \alpha_k v(i)^n$$

3.6

where *ncolum* is the number within the tower layer (see Figure 3.7)
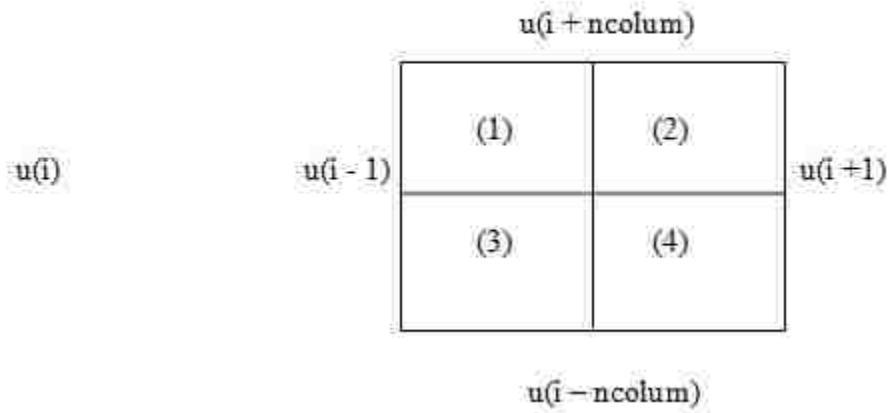


Figure 3. 7 Five point stencil (number in parenthesis denote element)

This first step reduces much of the anomalous divergence as possible. The number of passes through the smoothing step is determined empirically and is related to the relative atmospheric stability at that layer. The divergence is checked using the relative error, $\varepsilon$:

30

$$\varepsilon = u(i)^{n+1} - u(i)^{n} \quad \text{and} \quad \varepsilon = v(i)^{n+1} - v(i)^{n} \qquad\qquad 3.7$$

where n is the previous value and n+1 is the unknown value.

For convergence, max $\varepsilon \leq 10^{-4}$ should be satisfied. Once the solution is converged the smooth velocities are generated for this layer. If the solution is not converged, $u(i)^{n} = u(i)^{n+1}$, and $v(i)^{n} = v(i)^{n+1}$ and the program returns to equations 3.5 – 3.6 until convergence.

## 3.7 Upper Layer Windfield Generation

Accurately calculating the vertical velocity based on the velocity at the tower layer is difficult. In early times, most used $r^{-1}$ weighting to produce a smooth upper layer windfield (Sherman, 1978; Pepper and Brueckner, 1992). In this study, boundary layer technique is used to obtain the windfields at the upper layers. The top layer velocity is assumed to be constant, e. g. $U_{top}$ = 10 m/s and $V_{top}$ = 8 m/s. The following approach is used to get the upper layer values and top layer values.

## 3.8 Upper Layer Velocity Generation

To calculate the velocity at a grid point in the upper layer, the velocity of the grid point which has the same horizontal location on the tower layer and top layer are used through a simple linear equation (see Figure 3.8):
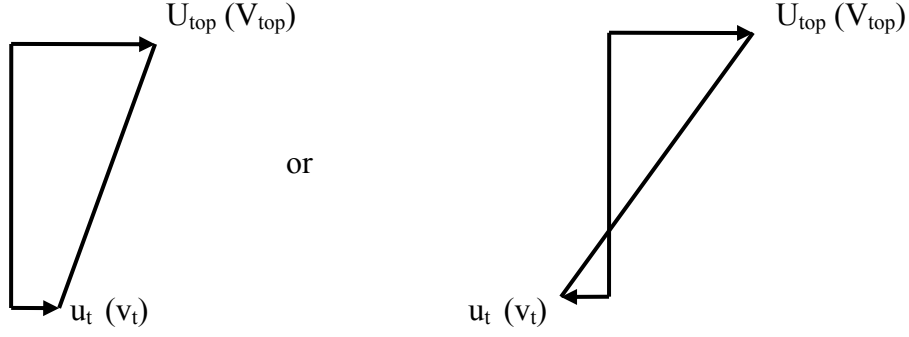
Figure 3. 8 Formulation of linear equation

Upper layer velocities are calculated from the following equations:

$$u(x, y, z) = \left(U_{top}(x, y, z_{top}) - u_t(x, y, z_{tow})\right)\frac{z - z_{top}}{z_{top} - z_{tow}} + U_{top}(x, y, z_{top}) \qquad 3.8$$

$$v(x, y, z) = \left(V_{top}(x, y, z_{top}) - v_t(x, y, z_{tow})\right)\frac{z - z_{top}}{z_{top} - z_{tow}} + V_{top}(x, y, z_{top}) \qquad 3.9$$

where (u, v) is the upper layer velocity, and ($u_t$, $v_t$) is the tower layer velocity.

## 3.9 Divergence Reduction of the Upper Layer

A slightly modified version of the three-point filter is used in this model to smooth the upper layer velocities. The new velocity at a given point is the average of the value at that point and at the two adjacent points in the vertical direction. The smoothing equation is:

$$u(i)^{n+1} = \frac{1}{3}\left(u(i)^n + u(i + ng)^n + u(i - ng)^n\right) \qquad 3.10$$

$$v(i)^{n+1} = \frac{1}{3}\left(v(i)^n + v(i + ng)^n + v(i - ng)^n\right) \qquad 3.11$$

where *ng* is the number of nodes on the ground ( for this case it is 7595 nodes).

Then divergence is given by:

$$\varepsilon = u(i)^{n+1} - u(i)^{n} \quad \text{and} \quad \varepsilon = v(i)^{n+1} - v(i)^{n} \qquad \text{3.12}$$

where $\varepsilon \leq 10^{-4}$ should be satisfied for convergence. A FORTRAN code was used to generate the initial surface wind velocities and the upper layer wind filed.

## 3.10 Generation of Vertical Velocity

The estimation of vertical velocities is one of the most difficult problems in the modeling of wind flow. Integration of the mass continuity equation using the large scale horizontal wind observations and then accounting for divergence correction is the simplest method for the computation of the vertical velocities.

The equation of continuity is:

$$\frac{\partial u}{\partial x} + \frac{\partial v}{\partial y} + \frac{\partial w}{\partial z} = 0. \qquad \text{3.13}$$

In this study, the vertical velocities are calculated using a simple difference version of equation 3.13, which is given as:

$$\frac{u(i+1) - u(i-1)}{x(i+1) - x(i-1)} + \frac{v(i+ncolum) - v(i-ncolum)}{y(i+ncolum) - y(i-ncolum)} + \frac{w(i) - w(i-ng)}{z(i) - z(i-ng)} = 0 \qquad \text{3.14}$$

Then the vertical velocities are obtained from:

$$w(i) = w(i-ng) - \left( \frac{u(i+1) - u(i-1)}{x(i+1) - x(i-1)} + \frac{v(i+ncolum) - v(i-ncolum)}{y(i+ncolum) - y(i-ncolum)} \right) (z(i) - z(i-ng))$$

$$\text{3.15}$$

where *ncolum* is the number of column in the tower layer and *ng* is the number of nodes on the ground.

A FORTRAN subroutine is used to generate the vertical velocities at all the nodes from equation 3.15 and the horizontal velocity values, u and v.

## 3.11 Wind Field Adjustment

As described in Chapter 2, a 3-D mass consistent model was first developed for use in ADPIC (Lange, 1978). An integral function is defined by the general variational analysis formalism, whose extremal solution minimizes the variance of the difference between the observed and analyzed values, subject to physical constraints which are satisfied exactly or approximately by the analyzed values. Strong constraints are the subsidiary conditions to be satisfied exactly, and the approximately imposed conditions are the weak constraints. When the number of strong constraints is less than the number of weak constraints, a minimal solution exists. Subject to the strong constraint that the three-dimensional analyzed wind field is nondivergent, a function is needed for this model to minimize the variance of the difference between the adjusted and original values. The function is shown in Equation 2.18, which is:

$$E(u,v,w,\lambda) = \int_{\Omega} \left[ \alpha_1^2 (u-u_0)^2 + \alpha_1^2 (v-v_0)^2 + \alpha_2^2 (w-w_0)^2 + \lambda \left( \frac{\partial u}{\partial x} + \frac{\partial v}{\partial y} + \frac{\partial w}{\partial z} \right) \right] d\Omega ,$$

3.16

where $u$, $v$ and $w$ are the adjusted velocity components in the $x$, $y$ and $z$ directions respectively, $u_0, v_0$ $and$ $w_0$ are the values of the observed velocities, $\lambda$ $(x, y, z)$ is the Lagrange multiplier, and $\alpha_i$ are the Gauss precision moduli, where $\alpha_i^2 = 1/2\sigma_i^2$ ($\sigma_i$ are the observation tower errors and/or deviations of the observed field from the desired

adjusted field). Since apparent distinctions exist between the horizontal and vertical directions but not between x and y coordinates, the Gauss precision moduli are assumed identical for the horizontal directions (Sherman 1978). The distinctions between the horizontal and vertical directions can be large, but the distinction between x and y coordinates are minimal. The Euler-Lagrange equations, the solutions of which will minimize the equation, are:

$$u = u_0 + \frac{1}{2\alpha_1^2} \frac{\partial \lambda}{\partial x},$$
(3.17)

$$v = v_0 + \frac{1}{2\alpha_1^2} \frac{\partial \lambda}{\partial y},$$
(3.18)

$$\text{and } w = w_0 + \frac{1}{2\alpha_2^2} \frac{\partial \lambda}{\partial z},$$
(3.19)

and the continuity equation is:

$$\frac{\partial u}{\partial x} + \frac{\partial v}{\partial y} + \frac{\partial w}{\partial z} = 0.$$
(3.20)

By differentiating equations $3.17 - 3.19$ and substituting the results in the continuity equation we can obtain the equation for $\lambda$, which is a Poisson equation for $\lambda$:

$$\frac{\partial^2 \lambda}{\partial x^2} + \frac{\partial^2 \lambda}{\partial y^2} + \left(\frac{\alpha_1}{\alpha_2}\right)^2 \frac{\partial^2 \lambda}{\partial z^2} = -2\alpha_1^2 \left(\frac{\partial u_0}{\partial x} + \frac{\partial v_0}{\partial y} + \frac{\partial w_0}{\partial z}\right)$$
(3.21)

35

The appropriateness of the final wind field is dependent on the specifications of the values of $\alpha_1$ and $\alpha_2$, though this technique produces a three-dimensional non-divergent wind field over complex terrain. Sherman (1978) showed that the assumption of zero initial velocities is reasonable if the atmospheric conditions are near neutral. This assumption is not a valid one when there is strong convective activity. The value of $(\alpha_1/\alpha_2)^2$ should be proportional to the magnitude of the expected $(w/u)^2$. If it is smaller, then the horizontal adjustment dominates (Sherman, 1978) and if it is large, then the adjustment is predominantly in vertical component. We have taken the values of $\alpha_1$ and $\alpha_2$ as 0.01 and 0.1 respectively in this study.

### 3.12 Boundary Conditions of the Model

On the boundary, either the Lagrange multiplier, $\lambda$, or the normal velocity component should be zero. If we specify both, it over specifies the problem and violates the conditions for the uniqueness of the solution. The normal derivative of $\lambda$ is not zero, when $\lambda$ is zero at the boundary. Therefore equations 3.17 – 3.19 give an adjustment of the observed velocities. A non-zero adjustment of the velocity normal to the boundary implies mass entering and leaving the volume. For open or "flow through" boundaries, a boundary condition of $\lambda = 0$ is appropriate. Since the non-normal derivatives of $\lambda$ are zero, a constant value for $\lambda$ on an open boundary means no adjustment is made in the non-normal velocity.

The adjusted values of the normal velocity are the same as the observed value, when $\partial\lambda/\partial n = 0$ on the boundary. The normal velocity on the boundary will not be affected by setting $\partial\lambda/\partial n = 0$ on the boundary. There will be no transport of mass through the

boundary if the observed normal velocity is zero. Therefore $\partial\lambda/\partial n = 0$ means the boundary is closed or is a "no flow-through" boundary. Figure 3.9 shows the boundary conditions of the model.



$$\lambda = 0, \text{u} = U_{top}, \text{v} = V_{top}$$

$$\lambda = 0$$

$$\frac{\partial u}{\partial x} = \frac{\partial v}{\partial y} = \frac{\partial w}{\partial z} = 0$$

$$\lambda = 0$$

$$\frac{\partial u}{\partial x} = \frac{\partial v}{\partial y} = \frac{\partial w}{\partial z} = 0$$

$$\lambda = 0$$

$$\frac{\partial u}{\partial x} = \frac{\partial v}{\partial y} = \frac{\partial w}{\partial z} = 0$$

$$\frac{\partial \lambda}{\partial n} = 0, \text{u} = 0, \text{v} = 0, \text{w} = 0$$
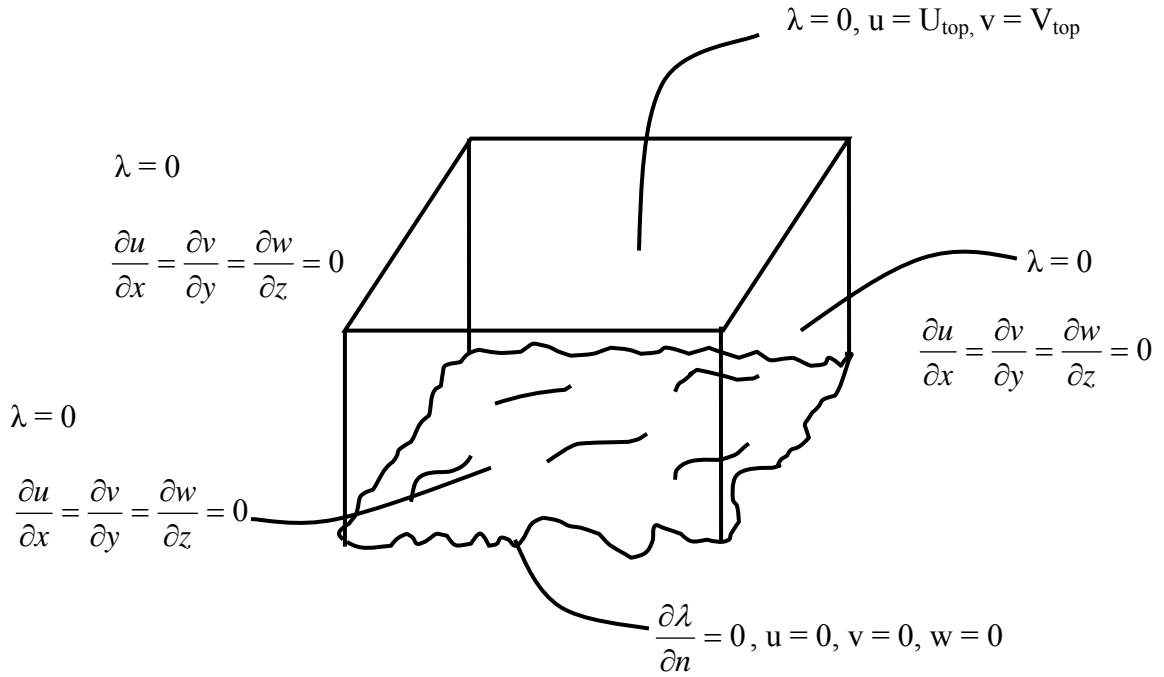
Figure 3. 9 Boundary conditions of the model

## 3.13 Finite Element Method Application

Applying the Galerkin weighted residuals technique to the Poisson equation (3.21) to solve for $\lambda$ (see equation 2.24 for more details), we get:

$$\int_{\Omega} N_i \left[ -\frac{\partial^2 \lambda}{\partial x^2} - \frac{\partial^2 \lambda}{\partial y^2} - \left(\frac{\alpha_1^2}{\alpha_2^2}\right)\frac{\partial^2 \lambda}{\partial z^2} - 2\alpha_1^2\left(\frac{\partial u_0}{\partial x} + \frac{\partial v_0}{\partial y} + \frac{\partial w_0}{\partial z}\right)\right] d\Omega = 0, \qquad 3.22$$

which can be written in matrix equivalent form as

$$\mathbf{K}\,\lambda = \mathbf{f}, \qquad\qquad 3.23$$

where, $\quad \mathbf{K} = \int_\Omega \left( \dfrac{\partial N_i}{\partial x} \dfrac{\partial N_j}{\partial x} + \dfrac{\partial N_i}{\partial y} \dfrac{\partial N_j}{\partial y} + \dfrac{\alpha_1^2}{\alpha_2^2} \dfrac{\partial N_i}{\partial z} \dfrac{\partial N_i}{\partial z} \right) d\Omega$ $\qquad$ 3.24

and $\qquad \mathbf{f} = 2\alpha_1^2 \int_\Omega N_i \left( \dfrac{\partial u_0}{\partial x} + \dfrac{\partial v_0}{\partial y} + \dfrac{\partial w_0}{\partial z} \right) d\Omega$ $\qquad$ 3.25

The relation has been "weakened" to a first order equation. The boundary condition flux of zero has been assumed for $\lambda$ automatically in the finite element procedure, which is an ideal value.

For the matrix solver, a Cholesky decomposition method is used to solve for hexahedral elements using 2x2x2 gauss point quadrature integration (2 points per direction).

## 3.14 Check of Divergence

Except for the tower and ground values, all the other velocity values are adjusted after calculating the $\lambda$ values using Equations 3.17 – 3.19. A divergence check is then performed, i.e.,

$$\varepsilon_u(i) = u(i) - u_0(i) \qquad\qquad 3.26$$

$$\varepsilon_v(i) = v(i) - v_0(i) \qquad\qquad 3.27$$

$$\varepsilon_w(i) = w(i) - w_0(i) \qquad\qquad 3.28$$

$$\varepsilon_\lambda(i) = \lambda(i) - \lambda_0(i) \qquad\qquad 3.29$$

If any one of these values exceed $\varepsilon_{max} > 10^{-4}$, then,

$u_0(i) = u(i), v_0(i) = v(i), w_0(i) = w(i), \lambda_0(i) = \lambda(i)$ and the solution returns to equation

3.22 until $\varepsilon_{max} \leq 10^{-4}$.


## 3.15 Methods of Computation

All the calculations were done using *Intel® Visual Fortran* Compiler. Tecplot was used to display the results. For the 3-D wind fields, the NELLISINIT.F code converged within 2 minutes before 50 time steps and the WIND3D.F code converged in about 20 minutes and after 650 time steps.


## 3.16 3-D Wind Fields over the Nellis Dunes

Figure 3.10 shows the 3-D wind fields over the Nellis Dunes for the month of April, 2008 at three different elevations (20 m, 50 m and 100 m). As can be observed from the figure, the velocity magnitude increases with the elevation and becomes smoother with the increase in altitude.

20 m

X - East West
Y - North South
Z - Altitude
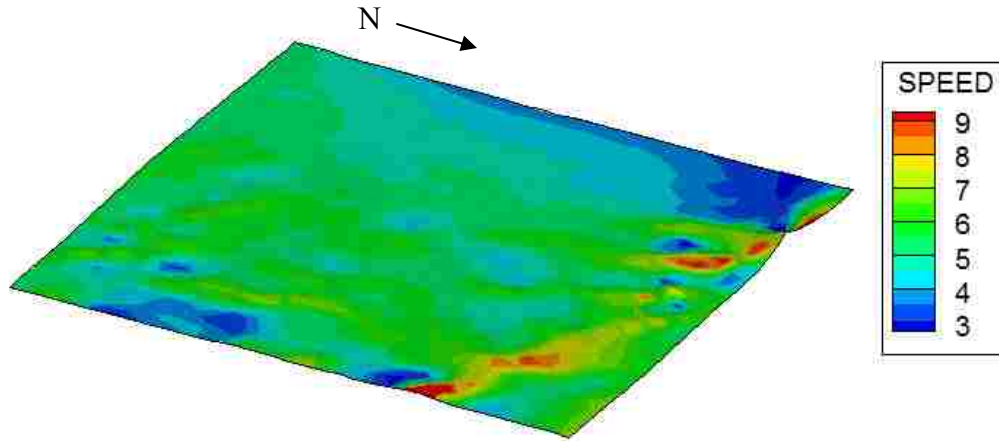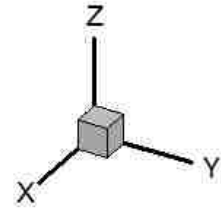


50 m

X - East West
Y - North South
Z - Altitude
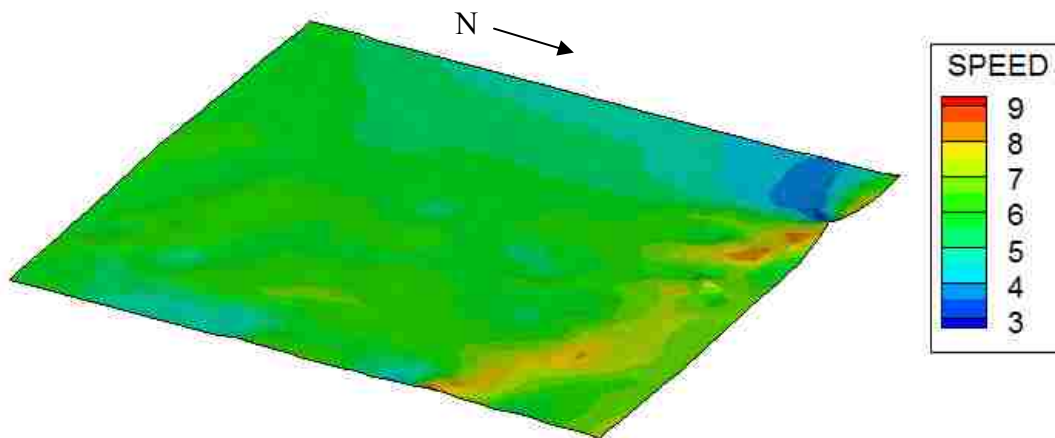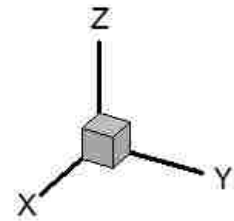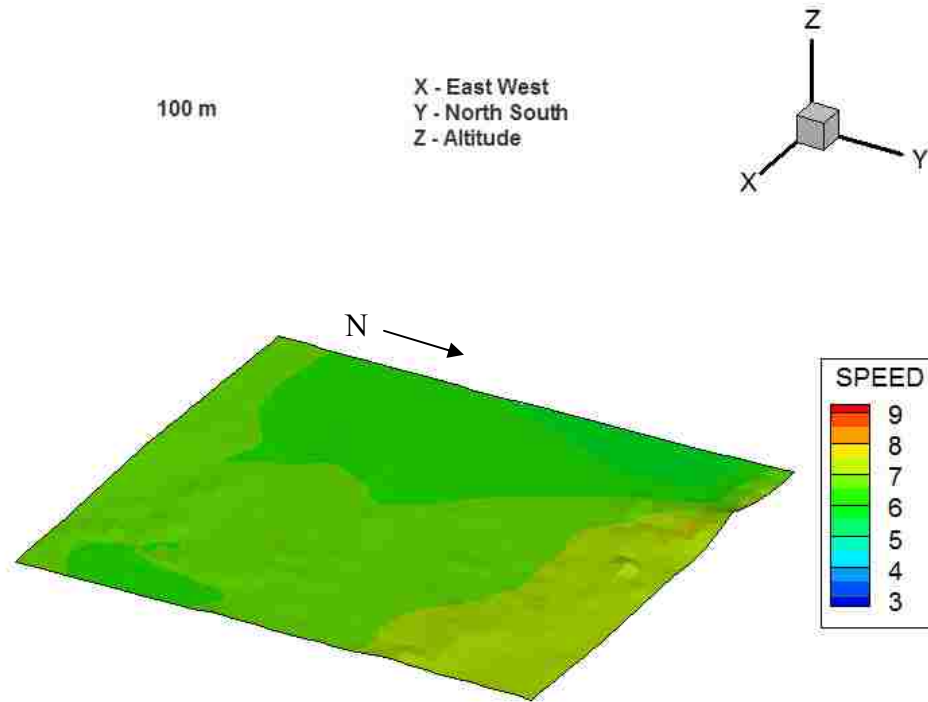
Figure 3. 10 3-D Wind fields at different height levels for April 2008

Figure 3.11 shows the wind vector plot of the entire Nellis Dunes area in the horizontal plane at 50 m.
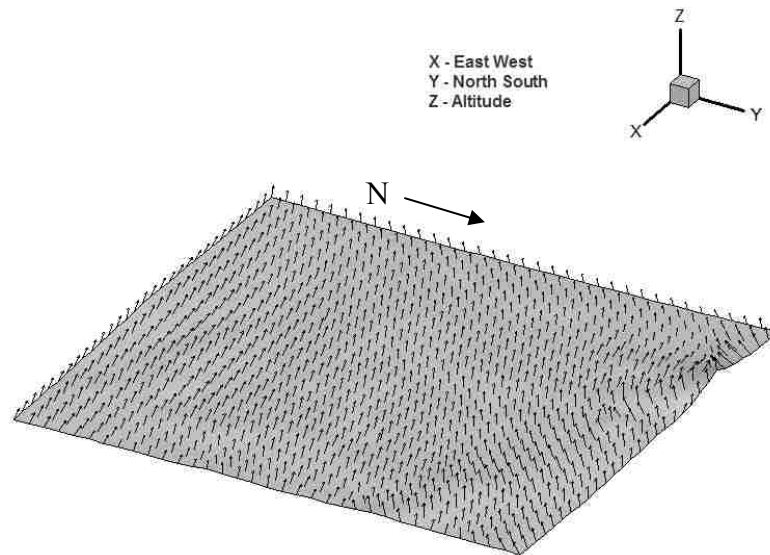


Figure 3. 11 Wind vector plot of the entire Nellis dunes area at 50 m

Figure 3.12 shows the 2-D monthly average wind speed for the entire Nellis Dunes for
two different heights (20 m and 50 m) for all the months.
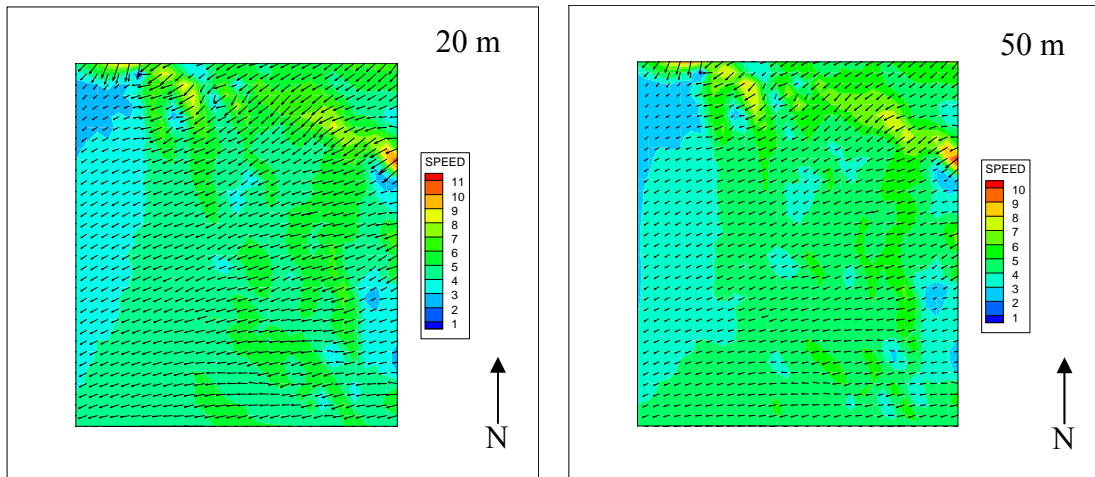


(a)  January
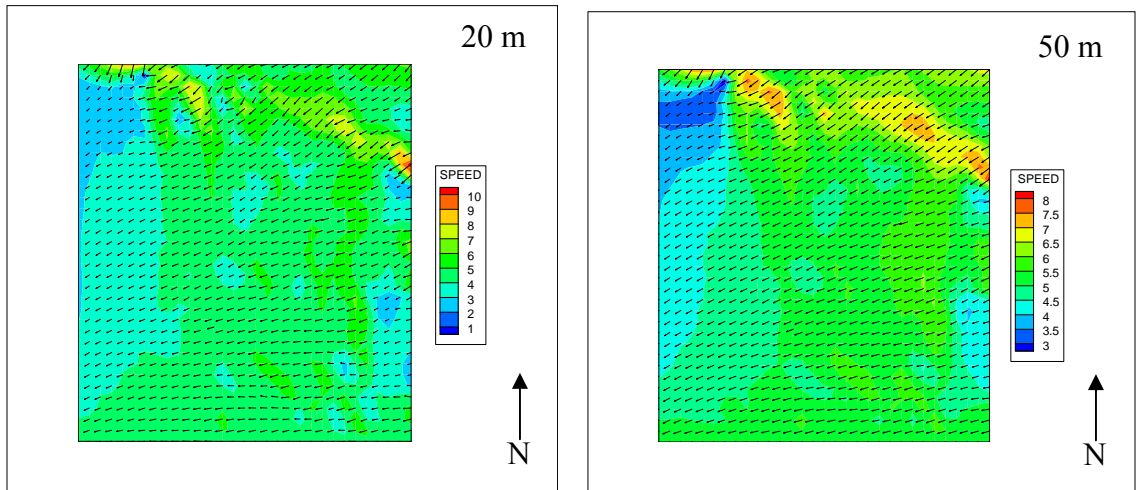


(b)  February
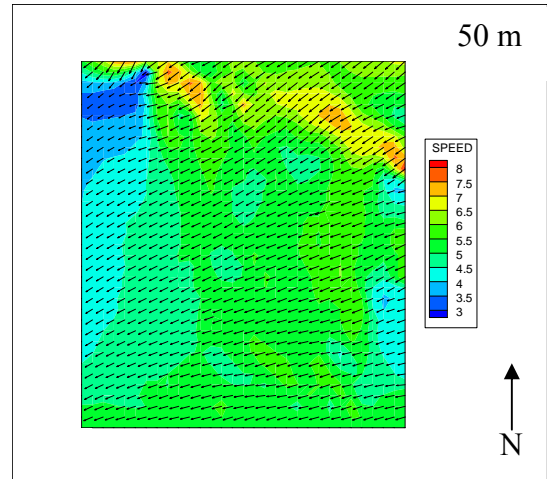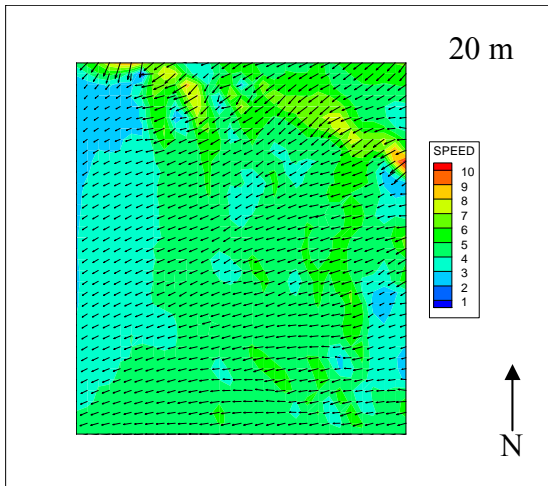
(c)  March
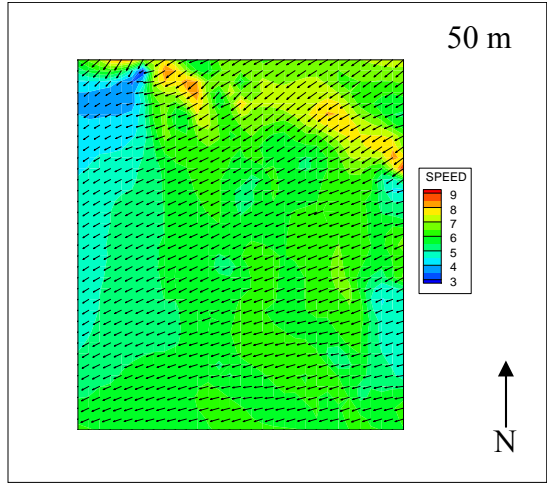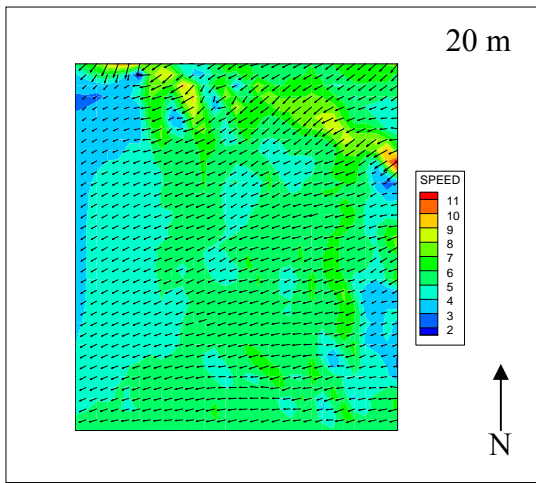


(d)  April
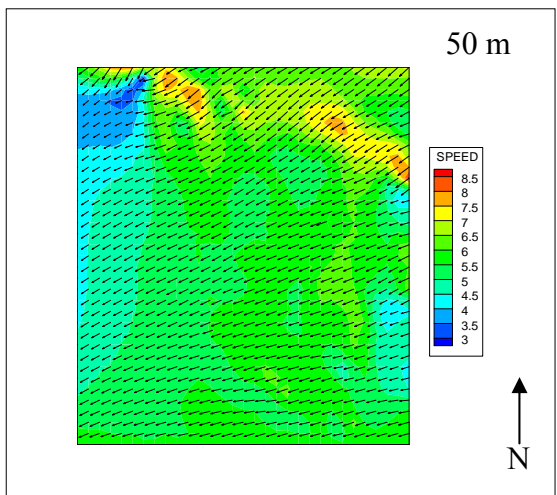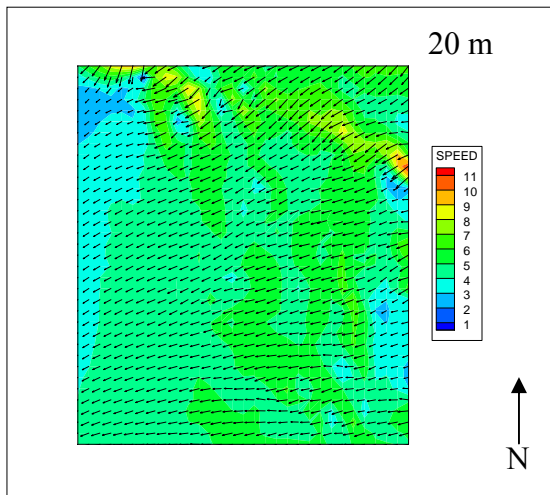


(e)  May
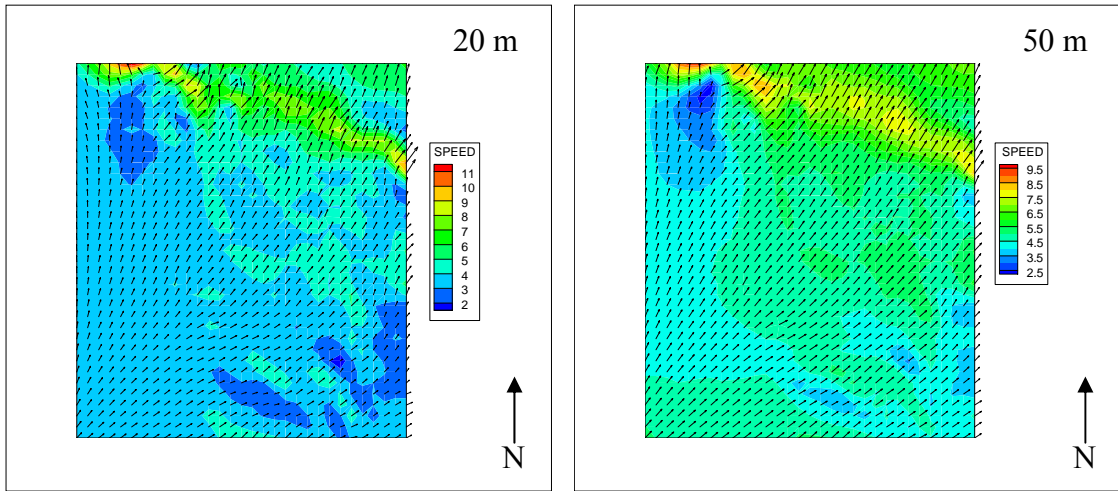
(f)  June
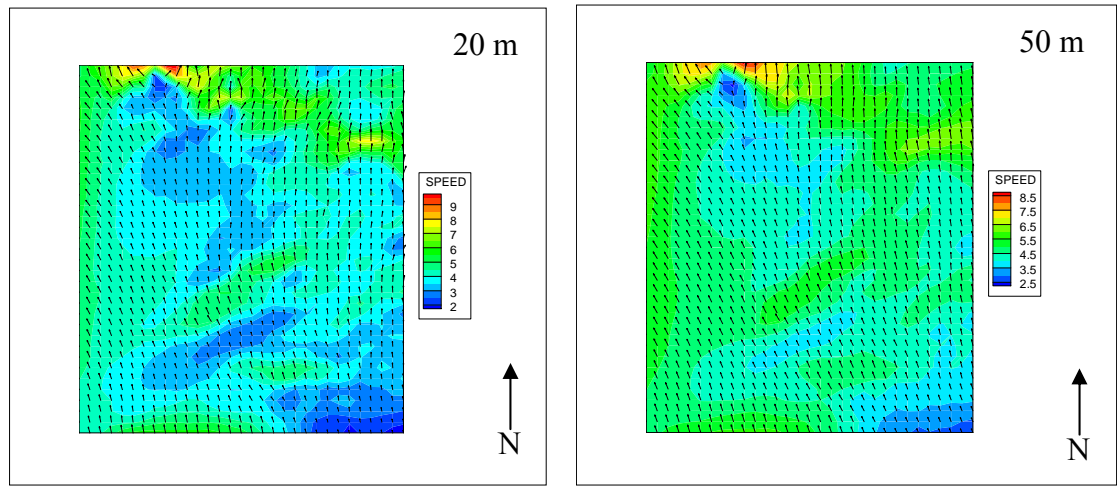


(g)  July
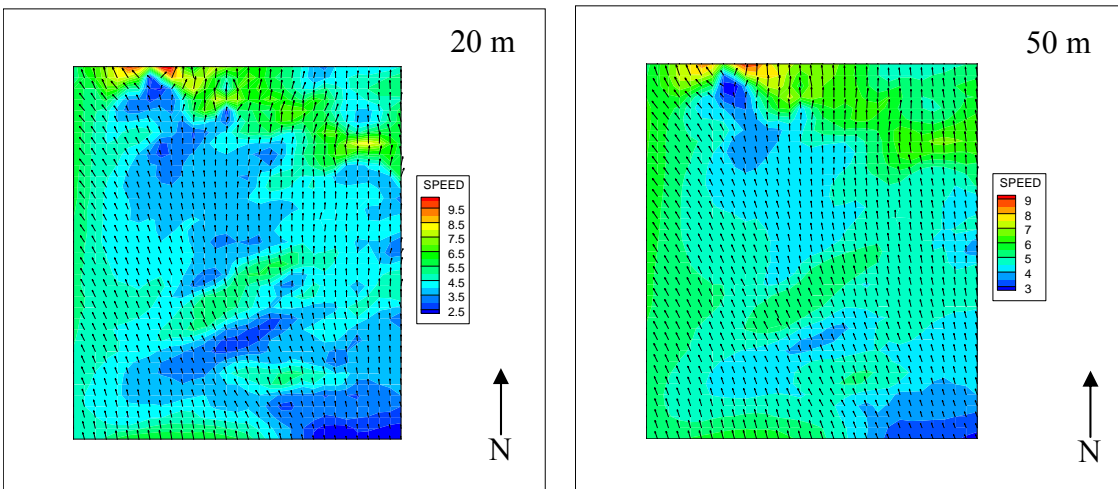


(h)  August
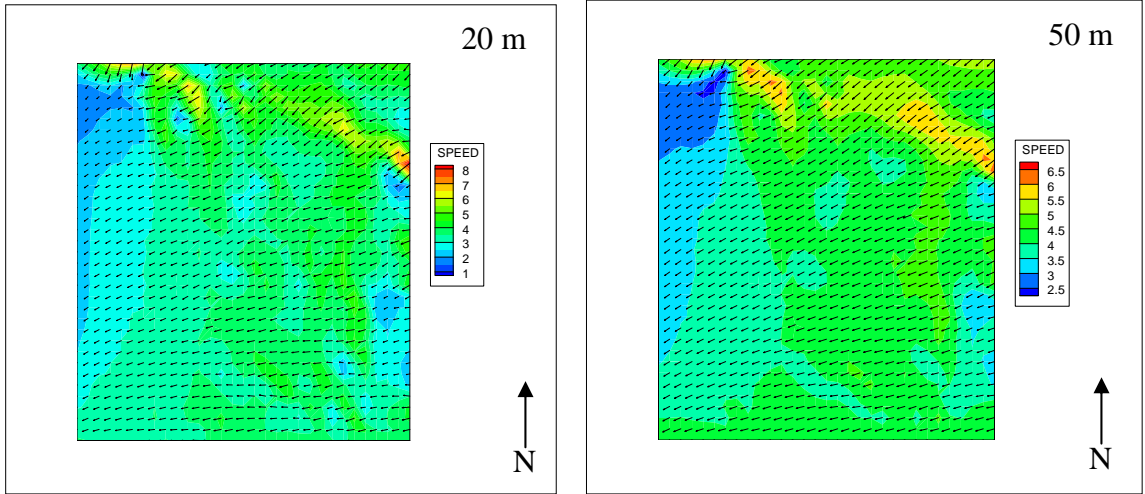
(i)    September



(j)    October



(k)    November

45
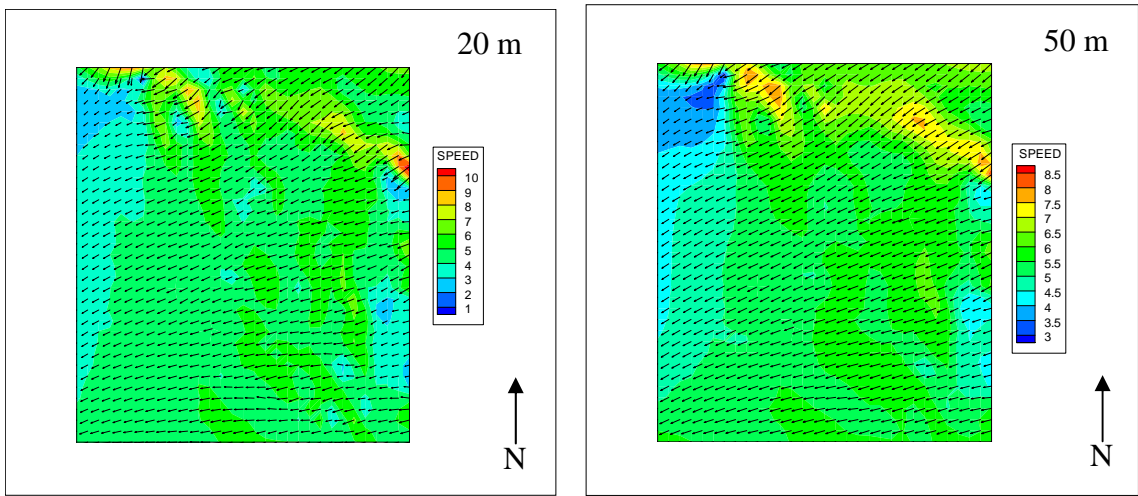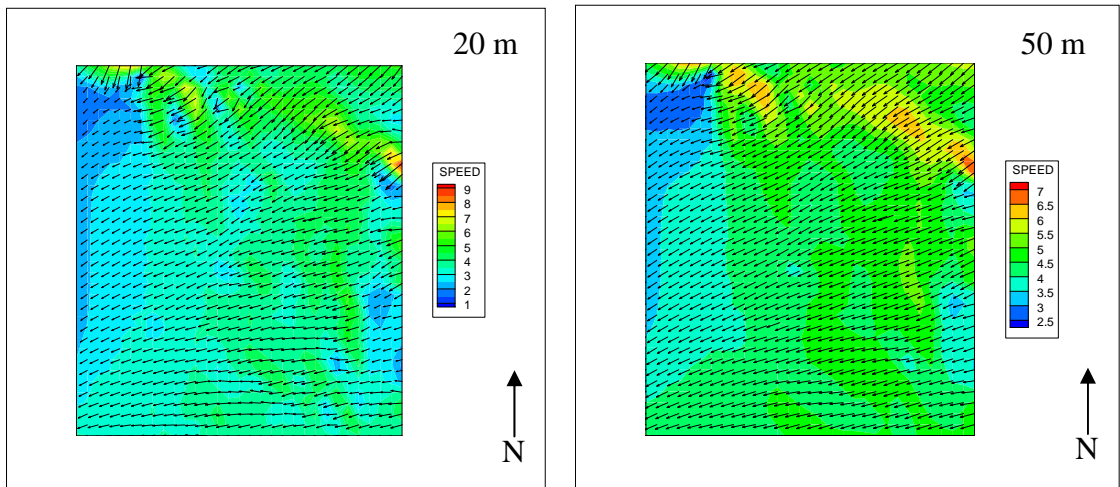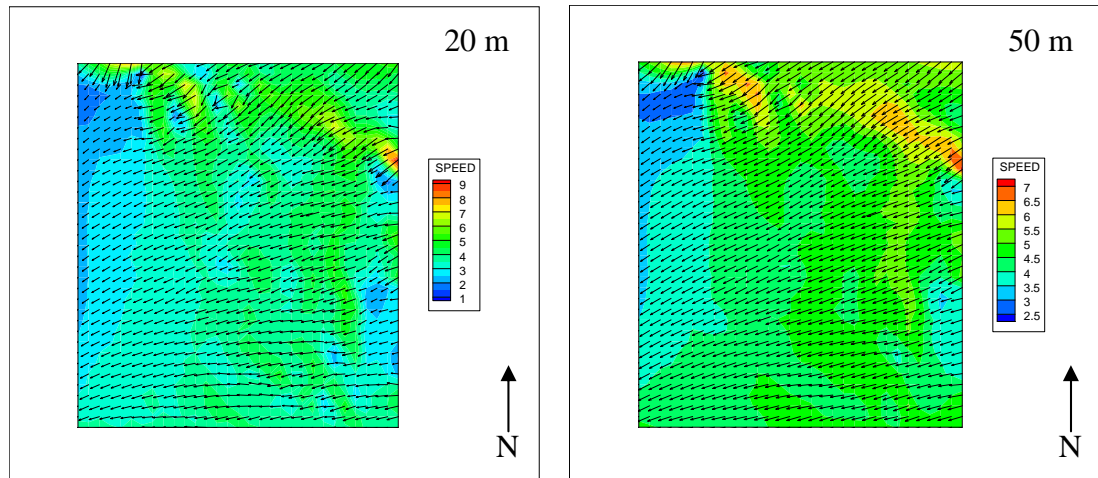
(l) December

Figure 3. 18    2-D Wind speed of Nellis dunes for 20 m and 50 m heights

**3.17 Comparison with Measured Data**

To validate model results, the calculated monthly average values were compared with recorded monthly average values at the 10 m tower which was located at N 3618457, W 11456214.   As shown in Table 3.1, wind velocities in the x and y directions were compared for the periods of August, 2008 to December, 2008. Overall good agreement can be observed.

Table 3.2Comparison with Measured Data at Tower 4

| Month | 10 Meter Tower Recorded (m/s) | | Simulation Results (m/s) | |
|---|---|---|---|---|
|  | Ux | Vy | Ux | Vy |
| August | 0 | 3.20 | -0.89 | 2.98 |
| September | -3.01 | -1.20 | -3.84 | -1.01 |
| October | -3.07 | -1.68 | -2.11 | -1.08 |
| November | -2.92 | -1.01 | -3.38 | -1.42 |
| December | -3.14 | -1.45 | -4.17 | -0.94 |

CHAPTER 4

WIND ENERGY ASSESSMENT

In the Southwestern U.S. wind energy is still a limited resource. Studies are still underway, but only several viable sites have been examined using local meteorological towers. The preliminary Wind Energy Atlas developed by NREL, MSOE and TrueWind solutions (AWS, Truewind) for the U.S. shows that Nevada has significant wind resource potential, but the estimation of wind energy resources is still under developed. Current assessment studies are preliminary, using relatively coarse meshes (~ 1-2 km) and do not include meteorological data from local towers. Due to the inaccessibility to reach remote ridges and mountain tops where the wind class may be higher (Class 3 or lower winds are common in most of the valleys), there has been very little detailed wind energy resource data for Nevada. The inability in obtaining appropriate wind data accumulated over the years within Nevada is one of the main problems in assessing wind power for Nevada.

Over the last few years, there have been major breakthroughs in wind energy, particularly in the improved assessment of the local wind resources and in the development of advanced wind turbine technology. There has been increased turbine efficiency with new blade technology along with improved rotor and generator speed using advanced power electronics. These enhancements have made wind turbines able to withstand greater wind loads and to capture more energy. Large scale wind power capabilities at around $0.05 per kWh have been made possible with the recent advances in the wind industry combined with the increased turbine capacity and size.

In this study, wind data collected from four sites are used to evaluate the wind energy potential of the Nellis Dunes area of Nevada. The monthly average data collected for the period of January 1$^{st}$, 2008 to October 17$^{th}$, 2008 were used to produce Weibull distributions of the wind and create Wind Rose diagrams. Wind speed and direction were recorded every 10 minute over the period from October 18$^{th}$, 2008 to February 1$^{st}$, 2009 for a dust dispersion study. This data was then converted to the monthly average format to produce Weibull distributions and Wind Rose diagrams. Since the data collected for the period October 18$^{th}$, 2008 to February 1$^{st}$, 2009 was averaged using 10 minute volumes, an MS Excel spreadsheet was used to convert the data to the monthly average format.

## 4.1 Wind Speed Distribution

Wind speed is the most critical data required to appraise the power potential of a candidate site since it has a cubic relation with the power. Wind speed is always unsteady over any site. The local land terrain, height above the ground surface and the weather system influence the wind speed at any site. Wind speed varies by the minute, hour, day season and year. Therefore to get confidence in assessing the energy-capture of a potential site, the annual wind field needs to be averaged over 10 or more years. However, it is not possible for most of the projects to wait that long and the long term measurements are expensive. In such situations, the "measure, correlate and predict (mcp)" technique is used, where the short term (say one year) data is compared with a nearby site having long term data (if available) to predict the long term annual wind speed at the site under consideration.

The wind pattern generally repeats over a period of one year, since it is driven by the sun and the seasons. To describe a wind site, most of the time the wind speed data averaged over the calendar months is used. For the brevity in reporting the overall "windiness" of various sites, sometimes the monthly data is aggregated over the year. A probability distribution function can be used to describe the wind-speed variations over a period of time.

## 4.2 Weibull Probability Distribution

In statistics and probability theory, the Weibull distribution (named after the Swedish Physicist W. Weibull, who used it to study the material strength in tension and fatigue in the 1930s) is a continuous probability distribution. Since the Weibull distribution closely mirrors the actual distribution of hourly wind speeds at many locations, it is used to describe the wind speed variations. Recently Azami et al.(2009) used the Weibull probability distribution to fit the wind speed data recorded for Malaysia. The results of their work using goodness-of-fit tests show that the Weibull distribution better suites the measured wind speeds. Weibull factor is often close to 2 and therefore a Rayleigh distribution can be used as a less accurate, but a simpler model.

Weibull probability distribution function 'h' with two parameters, the scale parameter 'c' and the shape parameter 'k' best describes the variation of wind speed (Wind and Solar Power Systems, Mukund Patel, 2006). The probability of wind speed being v at any time interval is given by the following relation:

$$h(v) = \left(\frac{k}{c}\right)\left(\frac{v}{c}\right)^{(k-1)} e^{-\left(\frac{v}{c}\right)^k} \qquad \text{for } 0 < v < \infty \qquad 4.1$$

In the probability distribution chart, h is plotted against v over a chosen period of time, where :

$$h = \frac{\textit{fraction of time the wind speed is between } v \textit{ and } (v + \Delta v)}{\Delta v} \qquad 4.2$$

From the probability function definition, the probability that the wind speed is between zero and infinity is unity, i.e.,

$$\int_0^\infty h * dv = 1 \qquad 4.3$$

The probability function can be expressed in terms of the number of hours in the year, if we choose the time period of one year, such that:

$$h = \frac{\textit{number of hours wind speed is between } v \textit{ and } (v + \Delta v)}{\Delta v} \qquad 4.4$$

If the unit for 'h' is the hours per year per meter per second, then the integral in Equation 4.3 becomes 8760 (the total number of hours in a year) instead of unity.
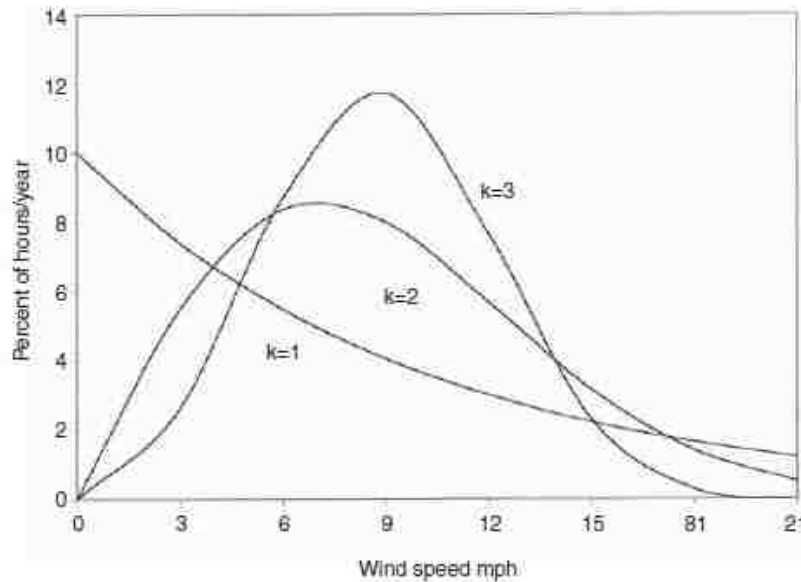


Figure 4.1 Weibull probability distribution function with scale parameter c = 10 and shape parameter k = 1, 2 and 3(courtesy Wind and Solar Power Systems, 2006)

50

Figure 4.1 shows a plot of h versus v for three different values of k. The left side curve with k = 1 has a heavy bias to the left where most of the days are windless    (v = 0). The right side curve, with k = 3, has a normal bell shape distribution, where the number of days with high wind speeds is equal to the days with low wind speeds. The middle curve with k = 2 is the wind speed distribution typically found in most of the sites. In this distribution, few days have high wind speeds and more number of days has lower speeds than the mean wind speed. Since the value of k determines the shape of the curve, it is called the 'shape parameter'. For greater values of c, the curve shifts to the right to the higher wind speeds. Therefore more number of days will have higher wind speeds, when the value of 'c' is higher. 'c' is called the scale parameter, since this shifts the distribution of hours at a higher number of speed scale.

When k = 1, the Weibull distribution is called an exponential distribution which is generally used in reliability studies. Weibull distribution approaches the normal distribution for k > 3, this is often called a Gaussian or bell-shape distribution. The wind speed at most of the sites has the Weibull distribution with k = 2, which is specifically known as a Rayleigh distribution. The actual measurement data taken from most sites compares very well with the Rayleigh distribution as shown in Figure 4.2. Therefore the Rayleigh distribution shows as a simple and relatively accurate representation of the wind speed with just one parameter, the scale parameter "c".
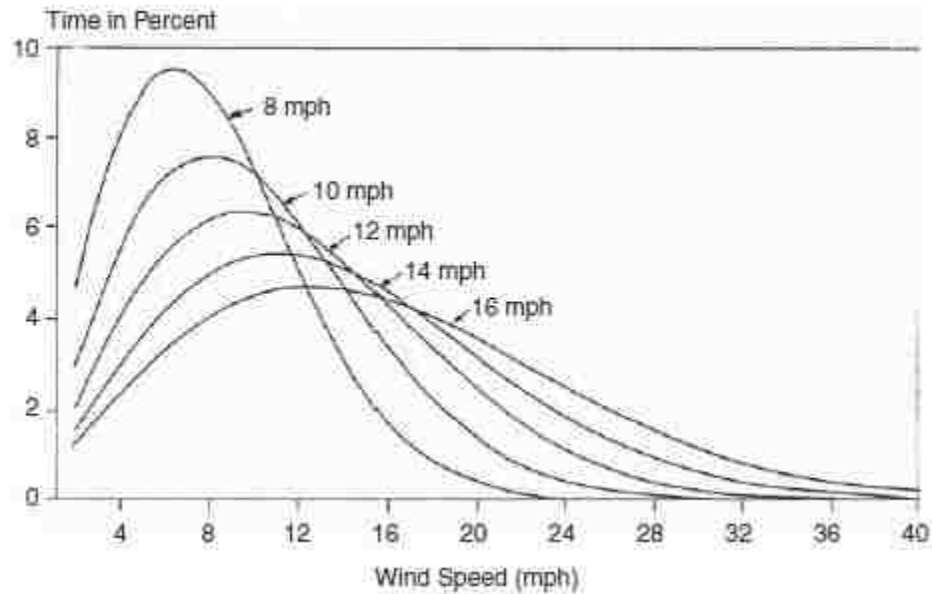
Figure 4.2 Weibull probability distribution with shape parameter k = 2 and the scale parameter ranging from 8 to 16 miles per hour (mph) (courtesy Wind and Solar Power Systems, 2006)

The Weibull probability distribution function characteristics are summarized as follows:

k = 1 makes it the exponential distribution, which is given as:

$$h = \lambda * e^{-\lambda V} \quad \text{where} \quad \lambda = 1/c$$

k = 2 makes it the Rayleigh distribution, which is given as:

$$h = 2\lambda^2 * V * e^{-(\lambda V)^2}, \text{ and}$$

k = 3 makes it a normal Gaussian or bell-shape distribution.

Most of the wind sites have a scale parameter ranging from 10 – 20 miles per hour (about 5 to 10 m / s), and have a shape factor ranging from 1.5 to 2.5 (rarely 3.0). Figure 4.3 compares the histogram with the Weibull distribution function for the month of November for the 20 meter height Tower 1(N 3617717, W 11455446). A statistical

52

software package called EasyFit was used to obtain the comparison. As can be seen, a good fit is found for the measured data; the values of scale parameter and shape parameter for the Weibull distribution used:

$$c = 4.9457, \text{ and}$$

$$k = 1.6266.$$
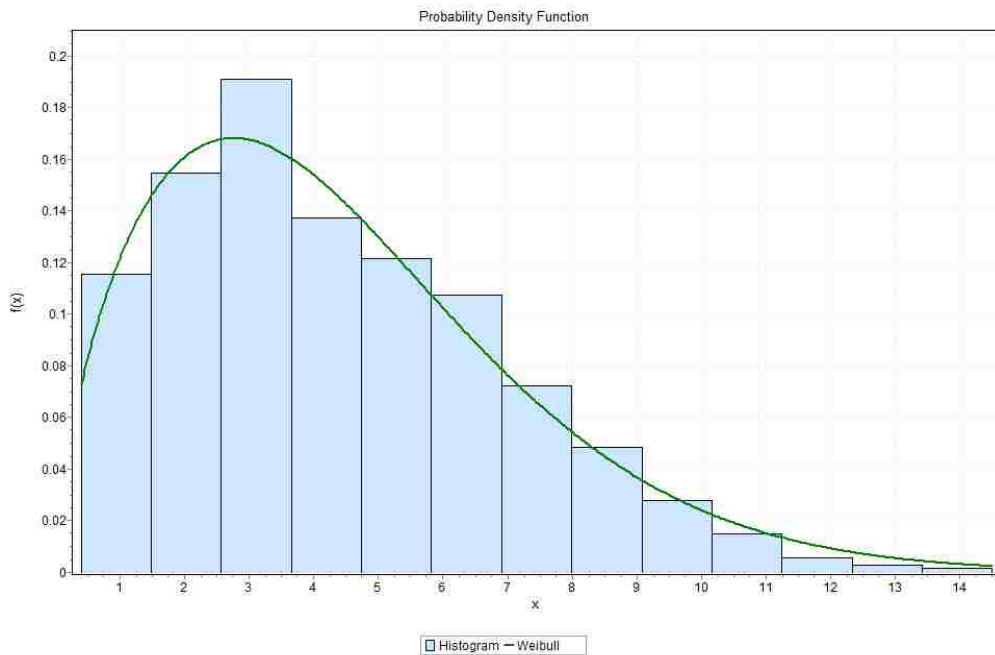


Figure 4.3  Comparison of wind histogram with the Weibull distribution function

Figure 4.4(a), (b), (c) shows the Weibull distribution plots for the month of April for three 20 meter towers.
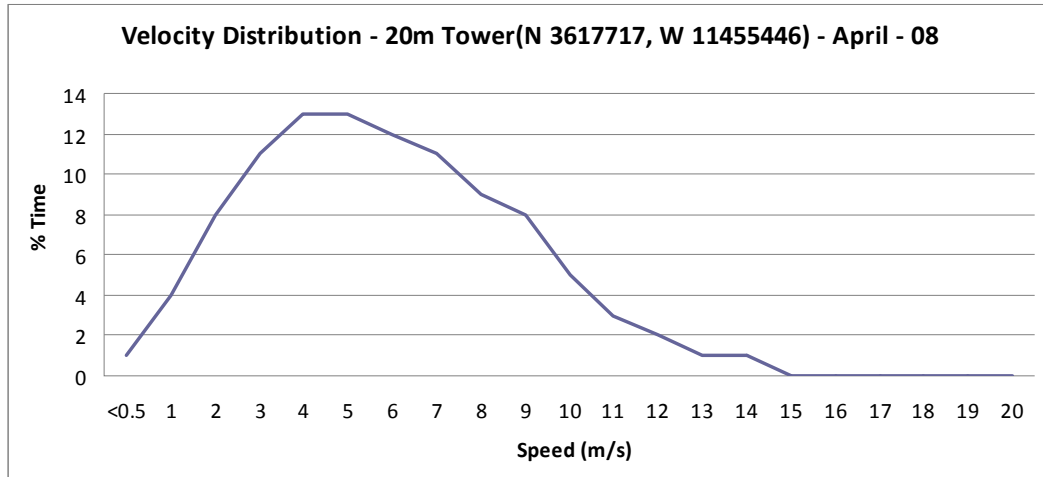
(**a**) Tower 1
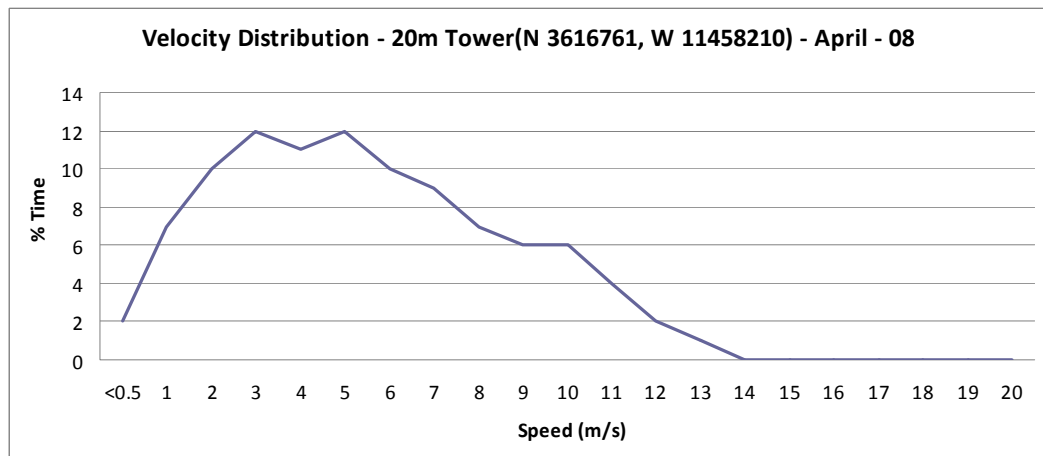


(b) Tower 2
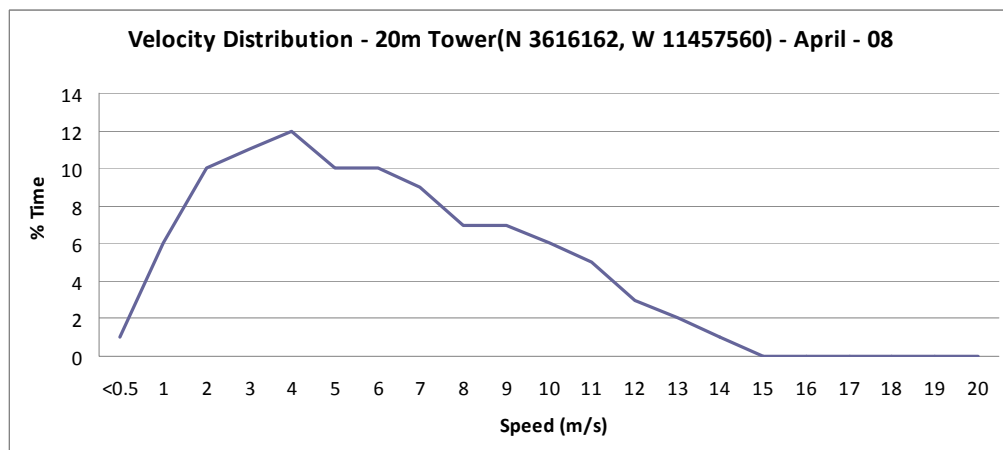


(c) Tower 3

Figure 4. 4 Weibull probability distribution for the month of April 2008

The Weibull distributions of the wind speed for the 12 month period staring January 2008 to December 2008, for all the three are shown in Figures 4.5. Since the fourth tower was vandalized and the data for the whole year was not available, it was not included in the Weibull distribution.

Tower 1 - January - 08



Tower 2 - January - 08



Tower 3 - January - 08



Tower 1 - February - 08



Tower 2 - February - 08



Tower 3 - February - 08



Tower 1 - March - 08



Tower 2 - March - 08



Tower 3 - March - 08

Tower 1 - April - 08



Tower 2 - April - 08



Tower 3 - April - 08



Tower 1 - May - 08



Tower 2 - May - 08



Tower 3 - May - 08



Tower 1 - June - 08



Tower 2 - June - 08



Tower 3 - June - 08

57

Tower 1 - July - 08



Tower 2 - July - 08



Tower 3 - July - 08



Tower 1 - August - 08



Tower 2 - August - 08



Tower 3 - August - 08



Tower 1 - September - 08



Tower 2 - September - 08



Tower 3- September - 08

58
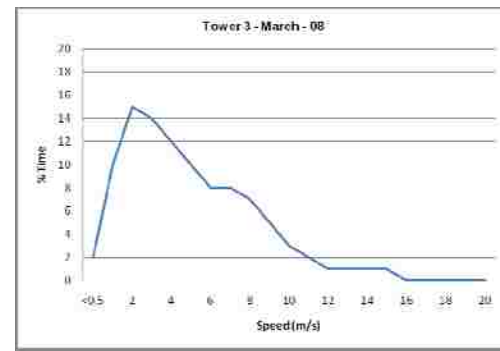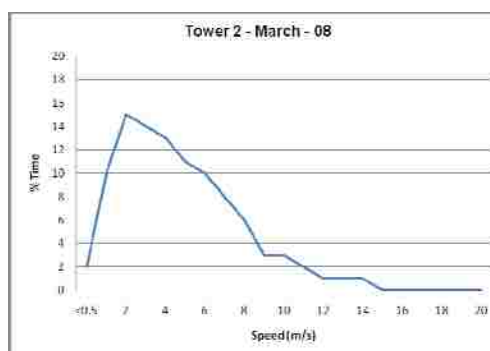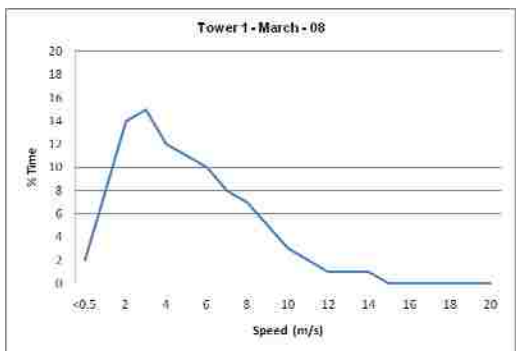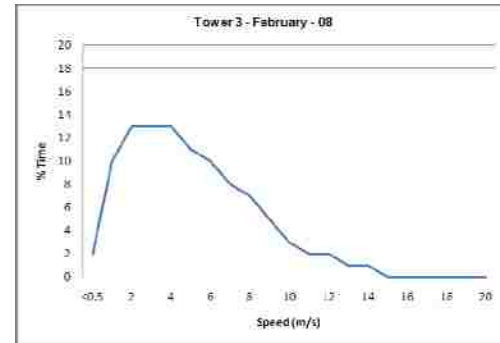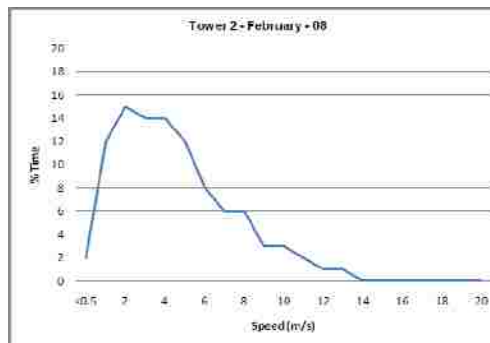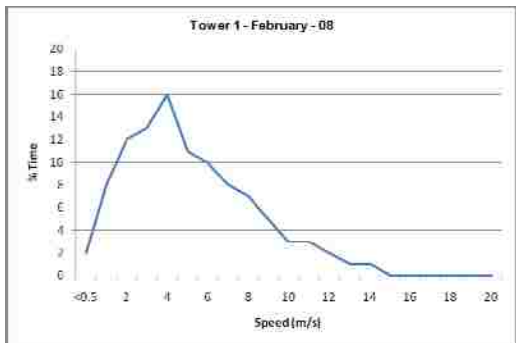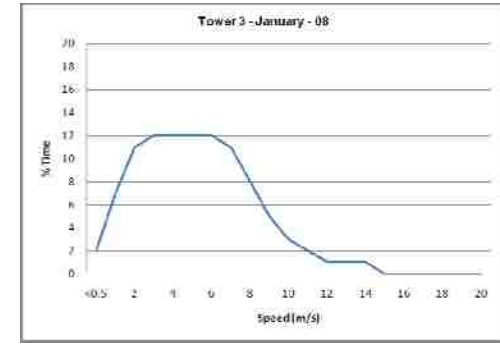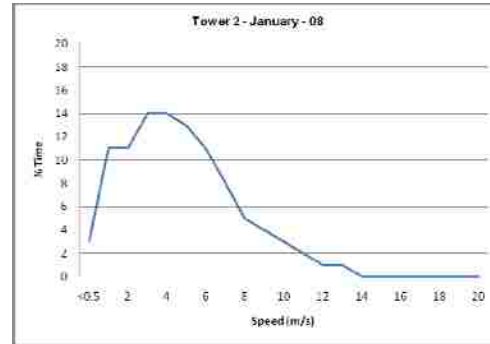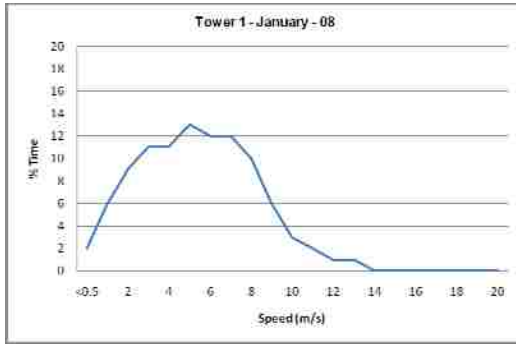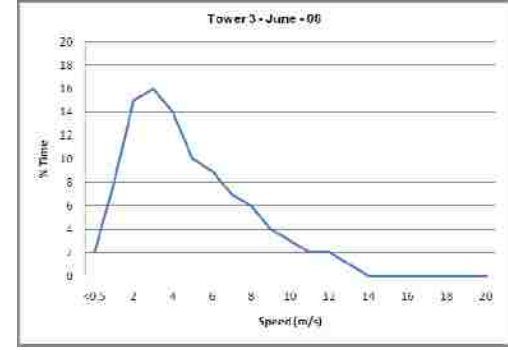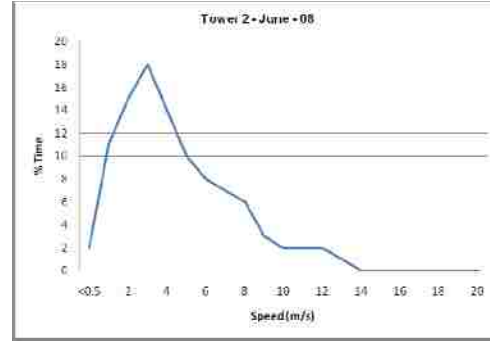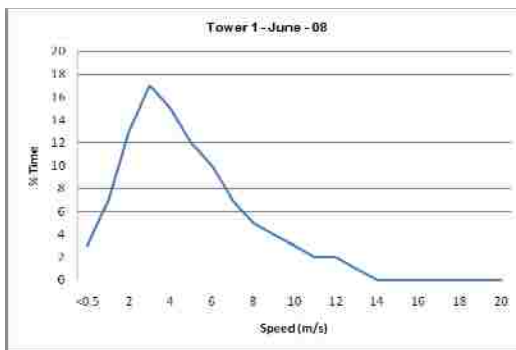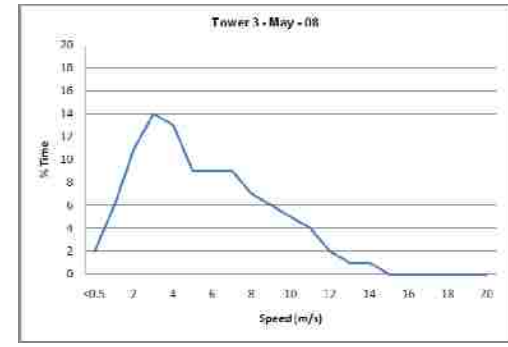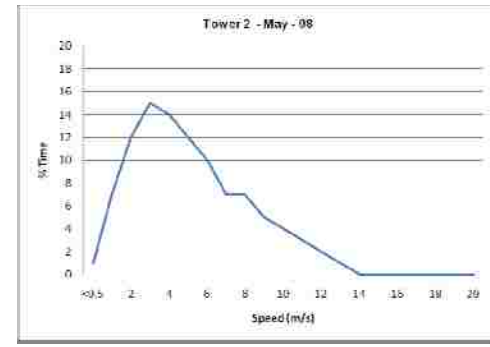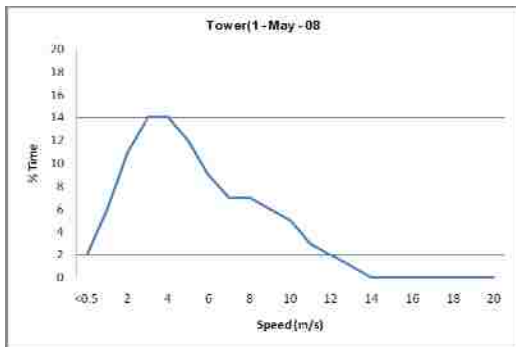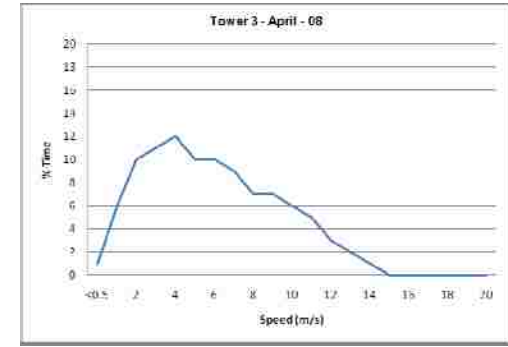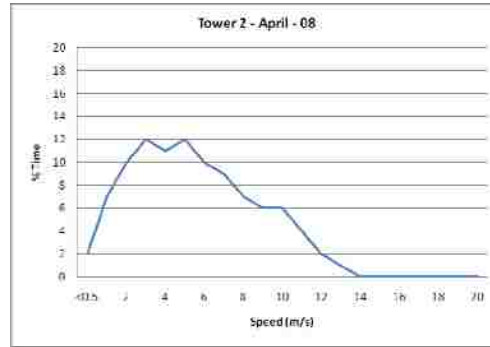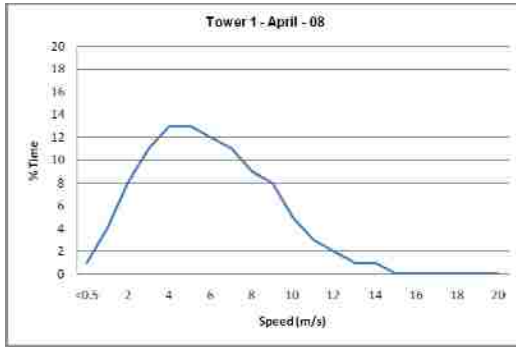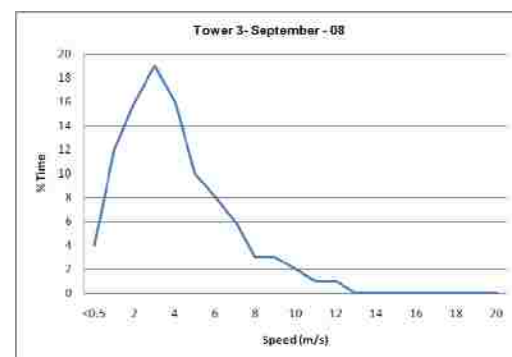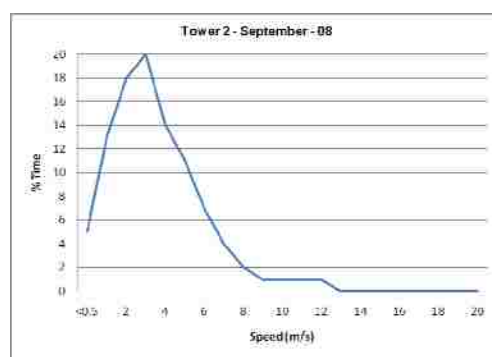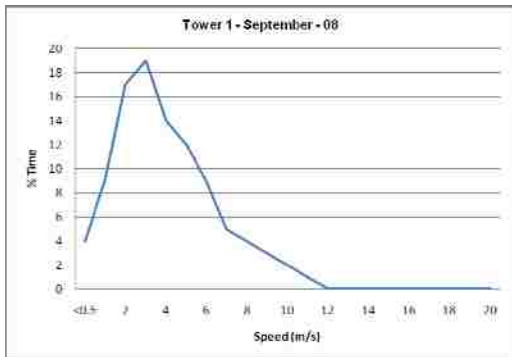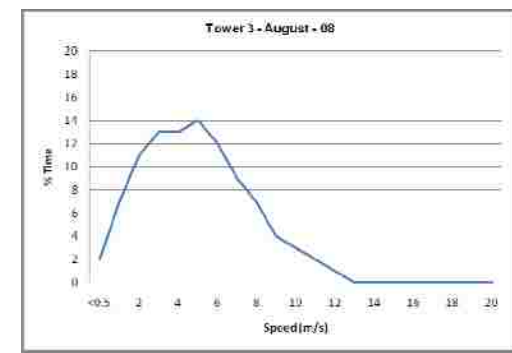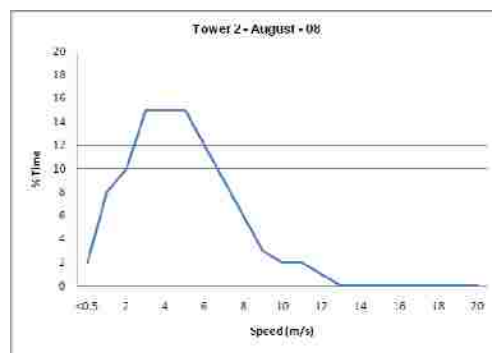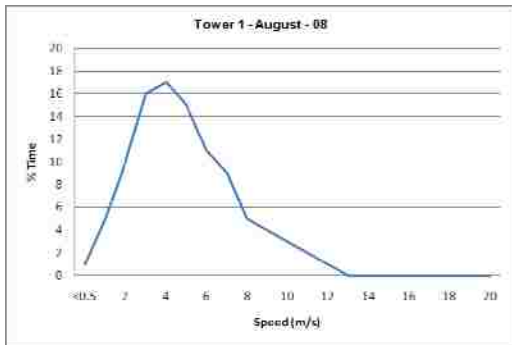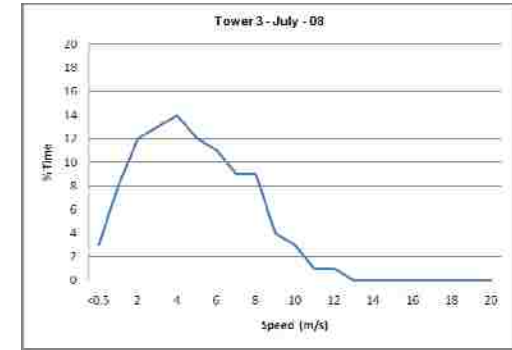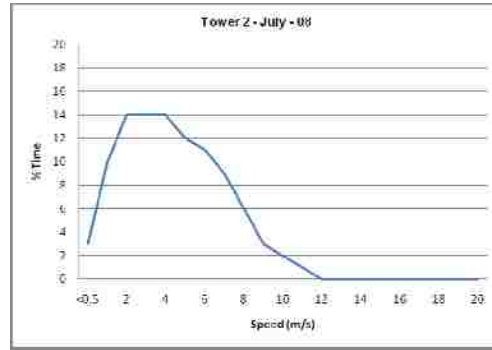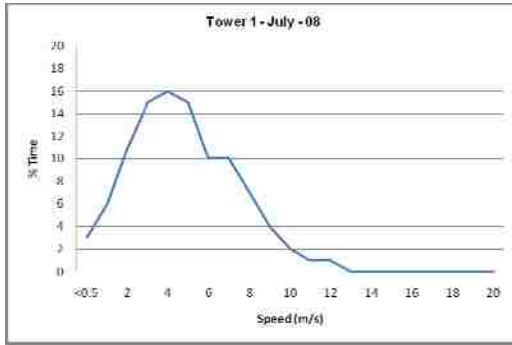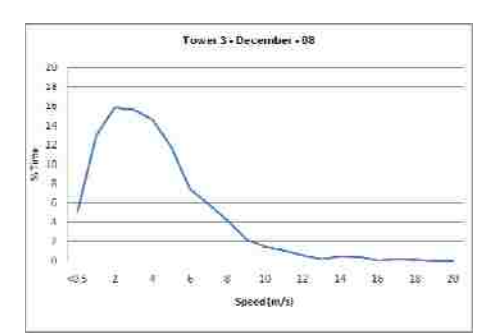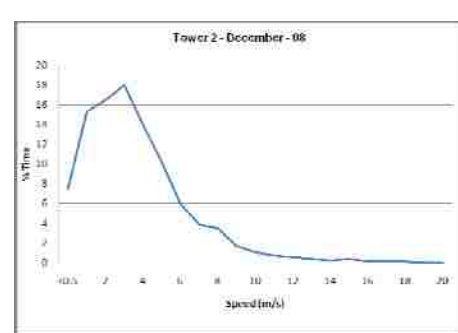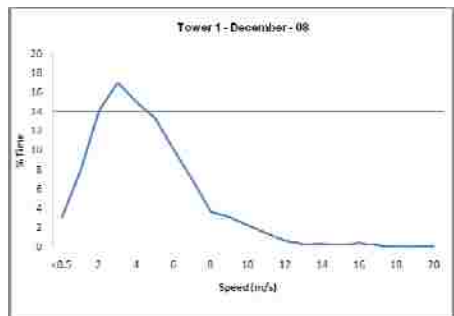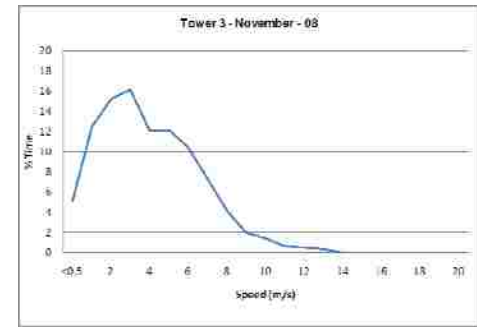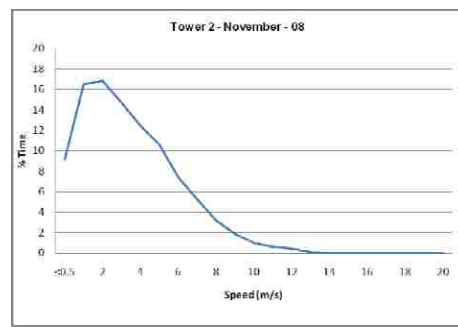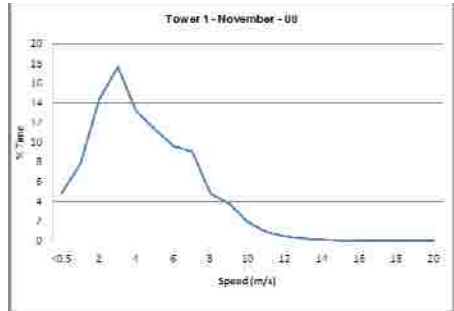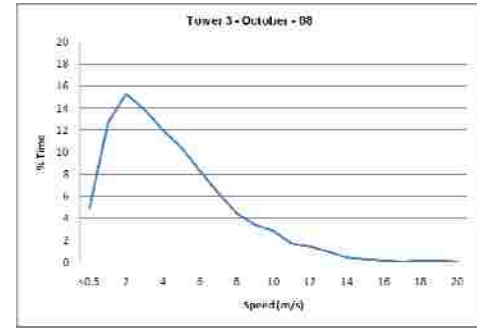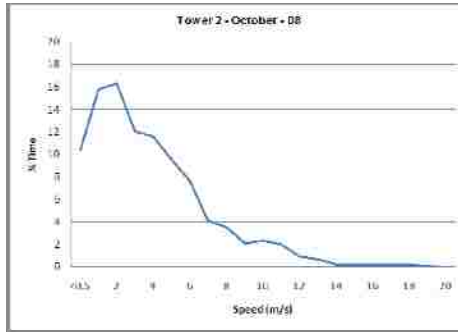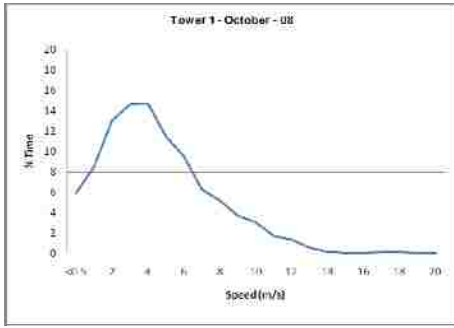
Figure 4.5  Velocity distribution diagrams

From Figure 4.5, it can be observed that the wind speed distributions for all the towers over the 12 month period show a good fit with the Weibull distribution.

**4.3 Wind Rose Diagram**

Since persistent strong winds usually come from a particular direction, meteorologists use the wind rose to graphically represent the distribution of wind speed and direction at a particular location. Historically wind roses are the predecessors of the compass rose (found on maps). Wind roses are extremely useful in siting wind turbines. If a large quantity of wind energy is coming from one particular direction, it is important to have as few obstacles as possible and as smooth a terrain as possible upstream of the turbine in that direction.

Wind roses were plotted using the polar coordinate system for the frequency of the wind over a long period of time. Modern wind roses are presented in a circular format showing the frequency of wind blowing from a particular direction. Each concentric circle represents a different frequency, emanating zero at the center to increasing frequencies at the outer circles. Typically the wind roses use 16 cardinal directions (N, NNE, NE, ENE, E, ESE, SE, SSE, S, SSW, SW, WSW, W, WNW, NW, NNW) and sometimes they are divided into 32 directions. In terms of angle of measurement in degrees, North corresponds to $0^o$/ $360^o$, East corresponds to $90^o$, South corresponds to $180^o$ and West corresponds to $270^o$.

In this study, the wind rose diagrams were drawn for all the four tower locations. In the wind rose diagram shown in Figure 4.6 (for the 20 meter tall tower, location N 3617717, W 11455446, for the month of January) each concentric circle represents a

different percentage of wind, emanating zero at the center to increasing percentages at the outer circles. For example, around 40% of the time the wind was flowing to the WestSouthWest direction (WSW), and around 10% towards NorthNorthEast (NNE). The total of the directional distribution is 100%.
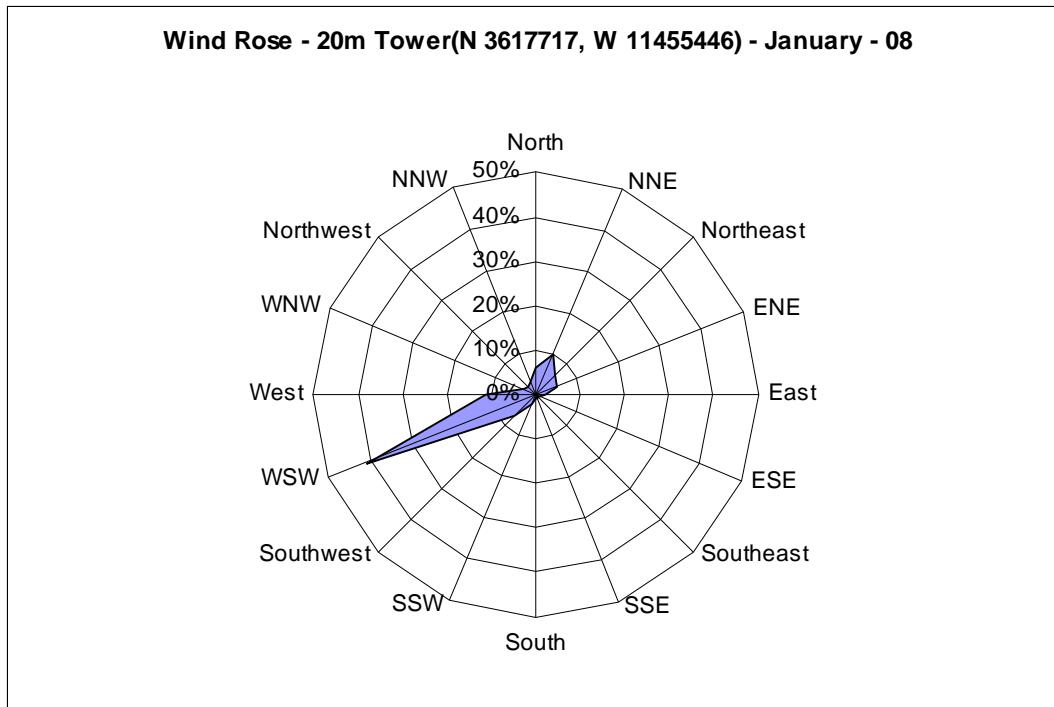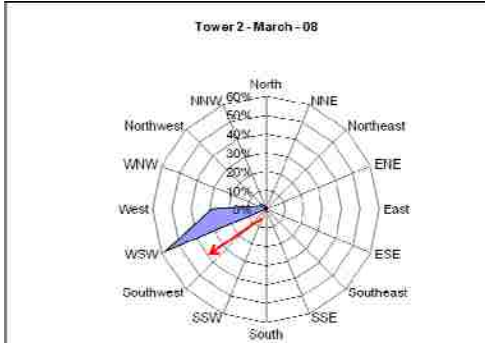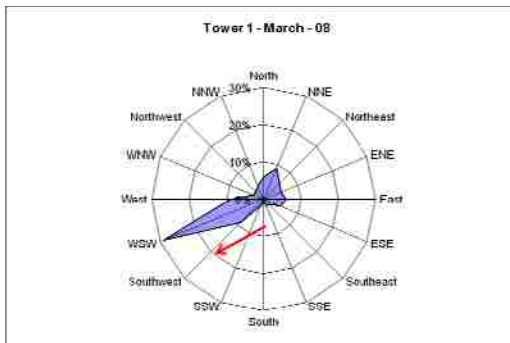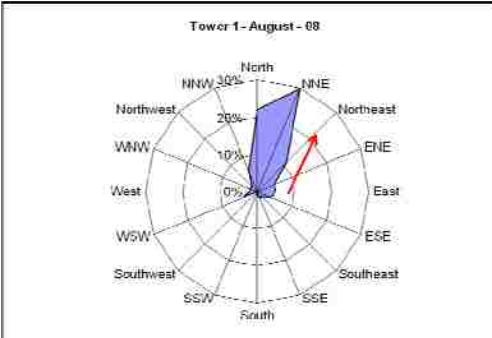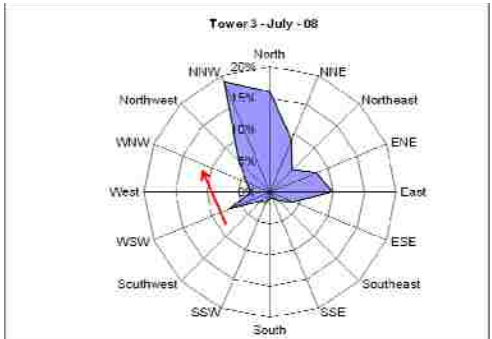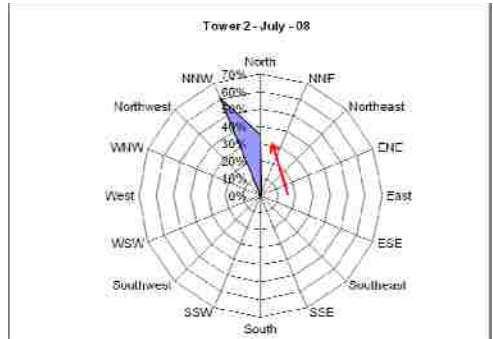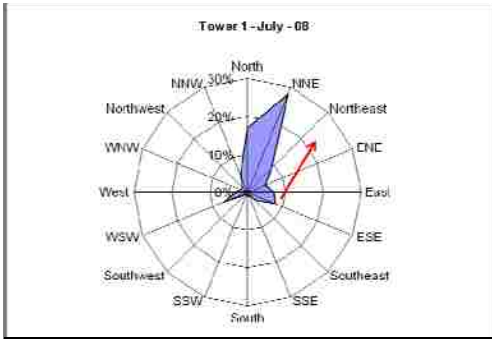


Figure 4.6 Wind rose for the month of January 2008 – Tower 1

The wind rose diagrams for the 12 month period staring January 2008 to December 2008, for all the three Towers are shown in the Figure 4.7. Since the fourth tower was vandalized and the data for the whole year was not available, it was not included in the Weibull distribution.
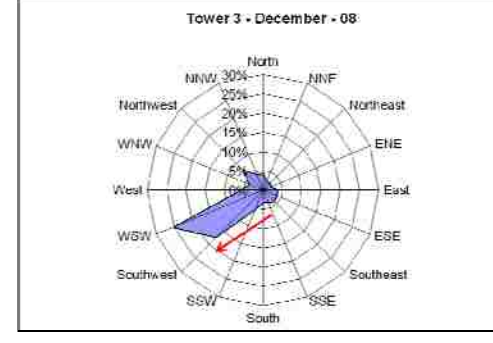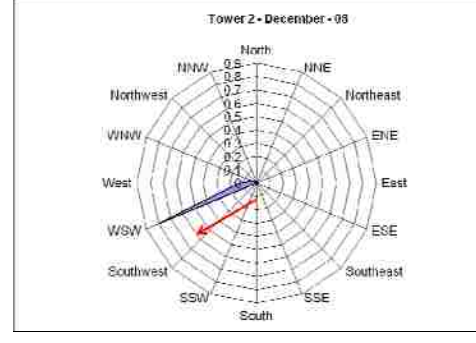
61

Tower 1 - January - 08
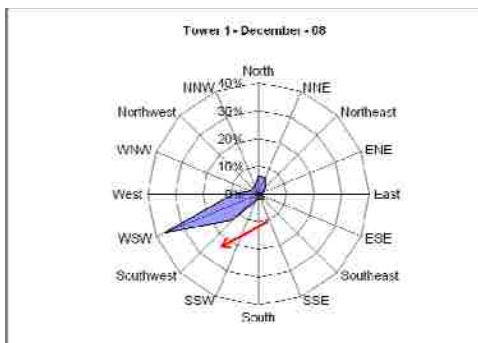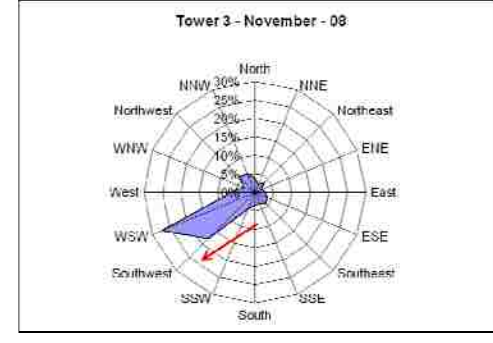


Tower 2 - January - 08



Tower 3 - January - 08



Tower 1 - February - 08



Tower 2 - February - 08



Tower 3 - February - 08



Tower 1 - March - 08



Tower 2 - March - 08



Tower 3 - March - 08

62
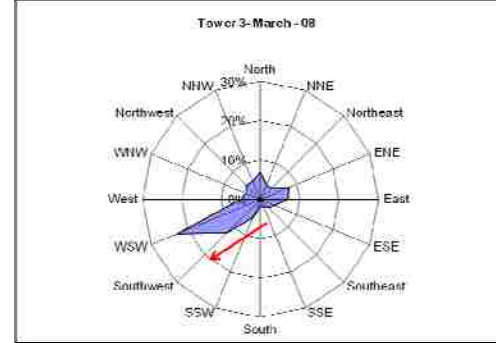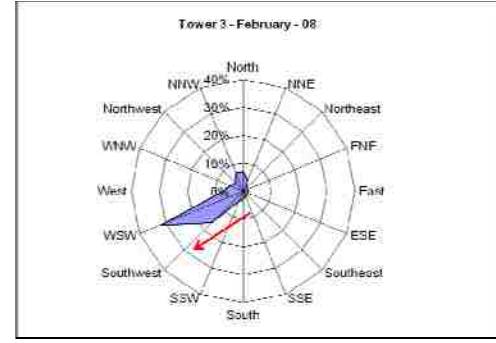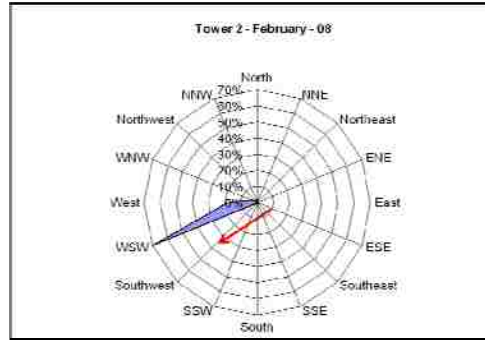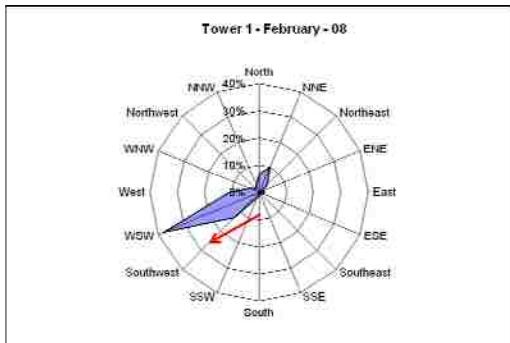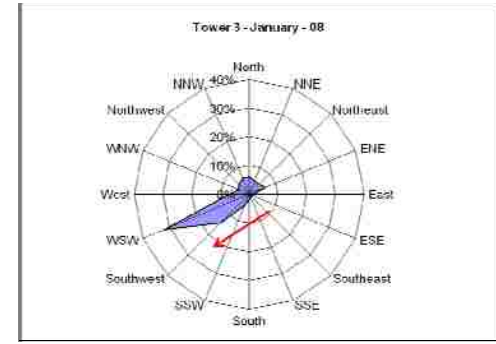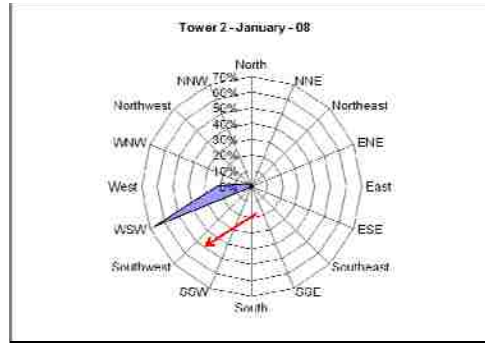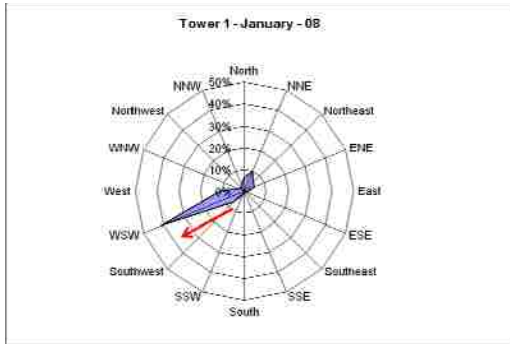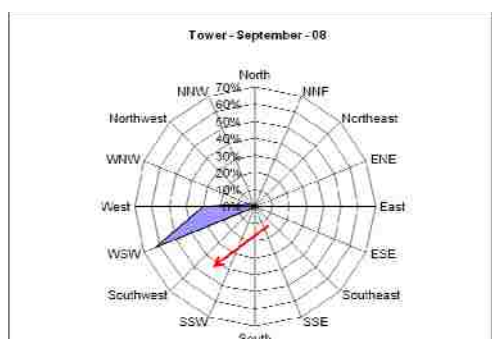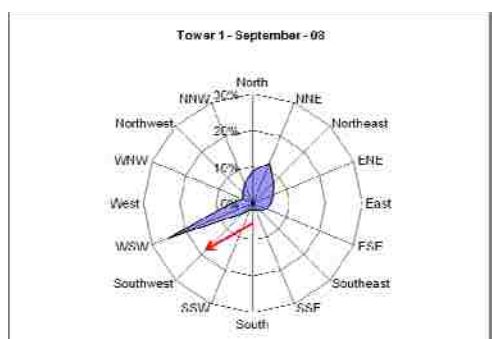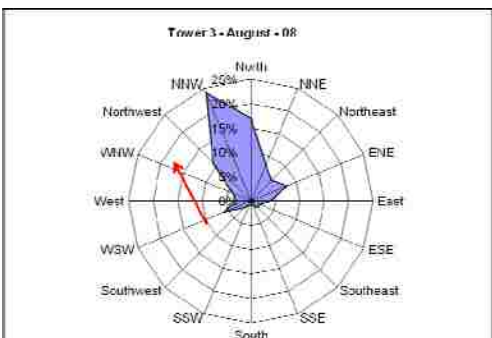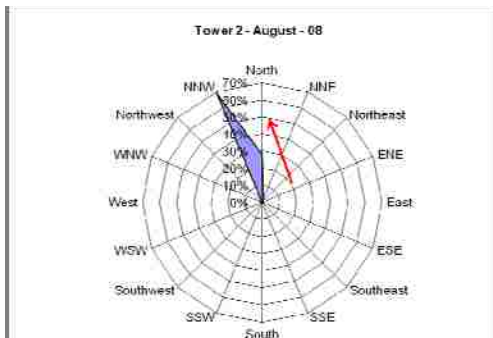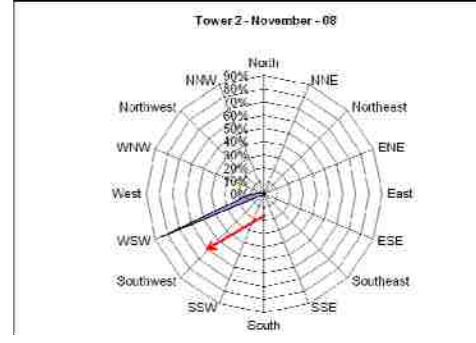
Figure 4.7   Wind Rose diagrams

**4.4 Wind Power Density**

In terms of the fossil-fuel displacement equivalency, the wind power potential accounts for about 0.65 of the total U.S. consumption (Pepper, 1998). Electricity potential from wind energy is estimated to be about 5,769 MW (Cormier, 1996) for Nevada.

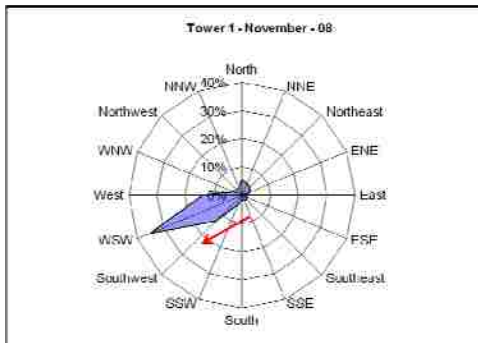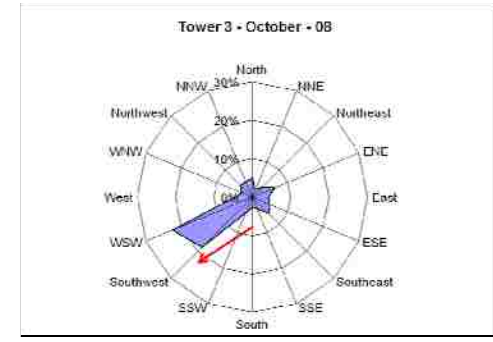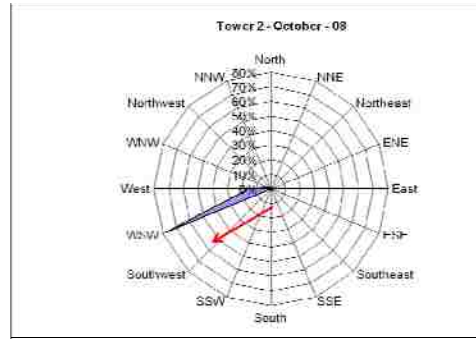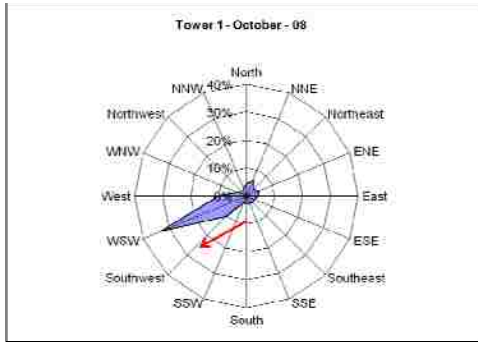The term "wind power classes' is a standard term of determining the suitability of a location for wind farm development. The wind power density indicates how much wind energy is available at the site for conversion by a wind turbine and is measured in watts per square meter. Based on the wind speed and available power per square meter, wind power is classified into seven different categories ranging from Class 1 (lowest) to Class 7 (highest). Class 4 winds are considered to be satisfactory for power generation and correspond to a wind speed of about 7 m/s (or around 320 – 400 Watts per square meter). More recently Class 3 winds are becoming potentially viable with evolving new wind turbine technology. Class 2 winds are marginal for utility-scale applications but may be suitable for small wind projects. Class 1 winds are generally not suitable for wind power development.

A vertical extrapolation of wind speeds based on the 1/7 power law is used in this classification. Wind speed generally increases 3% / 1000 m (5% / 5000 ft) of elevation. Battelle Wind Energy resource Atlas [20] is the source for this classification, and is shown in Table 4.1.

Table 4.1   Wind Power Classification

| Wind Power Class | 10 meter (33 ft) | | 50 meter (164) | |
| | Wind Power Density | Wind Speed Range m/s (mph) | Wind Power Density | Wind Speed Range m/s (mph) |
| --- | --- | --- | --- | --- |
| 1 | <100 | <4.4 (9.8) | <200 | <5.6 (12.5) |
| 2 | 100 – 150 | 4.4 (9.8) / 5.1 (11.5) | 200 - 300 | 5. 6 (12.5) / 6.4 (14.3) |
| 3 | 150 – 200 | 5.1 (11.5) / 5.6 (12.5) | 300 – 400 | 6.4 (14.3) / 7.0 (15.7) |
| 4 | 200 – 250 | 5.6 (12.5) / 6.0 (13.4) | 400 – 500 | 7.0 (15.7) / 7.5 (16.8) |
| 5 | 250 – 300 | 6.0 (13.4) / 6.4 (14.3) | 500 – 600 | 7.5 (16.8) /  8.0 (17.9) |
| 6 | 300 – 400 | 6.4 (14.3) / 7.0 (15.7) | 600 – 800 | 8.0 (17.9) / 8.8 (19.7) |
| 7 | >400 | > 7.0 (15.7) | >800 | >8.8 (19.7) |

The basis for calculating the wind energy potential comes from the relations of kinetic energy ($mV^2 / 2$) and momentum ($mV$). The wind power density for an average atmospheric condition can be calculated from:

$$WindPower / area = 0.5 \rho V^3$$

where the unit of power is Watts, the unit of area is $m^2$, the unit of wind velocity is m/s and the density of air is 1.225 kg/m$^3$ at sea level. The density of air at any elevation can be calculated from:

$$\rho = 1.225 - (1.194 * 10^{-4}) * Z$$

where Z is the location's elevation above sea level in meter.

In this study the wind power density is calculated using the hourly wind speed at each grid point, which is given as:

$$Speed_i = \sqrt{u_i^2 + v_i^2 + w_i^2} \qquad\qquad 4.5$$

The hourly wind power density at each grid point is then calculated from the relation:

$$WPD_i = 0.5 * \rho * Speed_i^3 \qquad\qquad 4.6$$

The monthly average wind power density is thus calculated using:

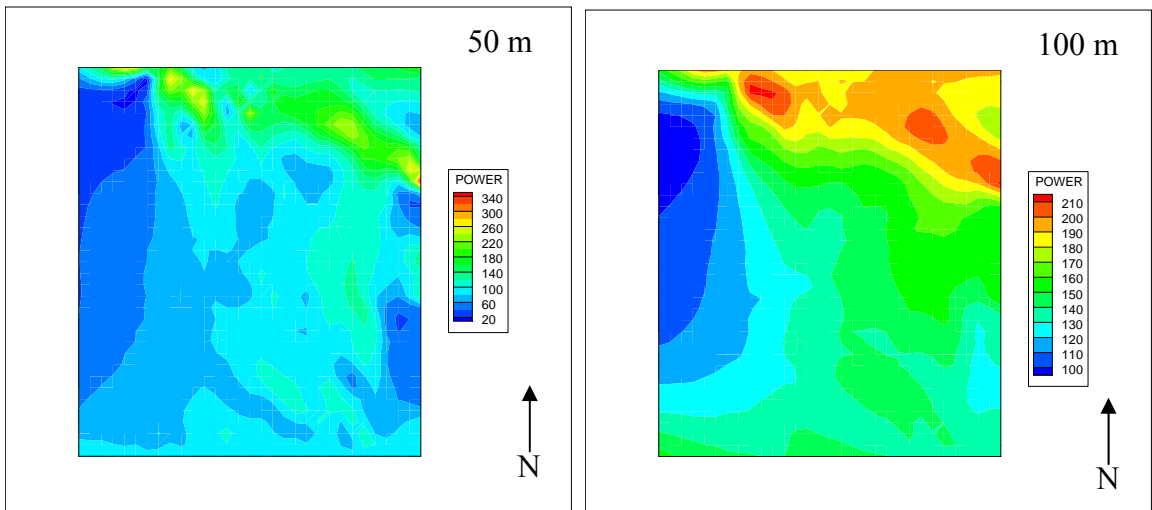$$WPD_{monthly\_avg} = \frac{\sum\limits_{i=1}^{N} WPD_i}{N} \qquad\qquad 4.7$$

where N is the total number of hours in a selected month.

The monthly wind power density maps were generated for the period January 1st, 2008 to December 31st, 2008 using Equations 4.5 – 4.7. Figure 4.8 shows the 2-D view of the monthly wind power densities for the period of January, 2008 to December, 2008 at 50 m and 100 m heights. The units of wind power densities are W / m$^2$.
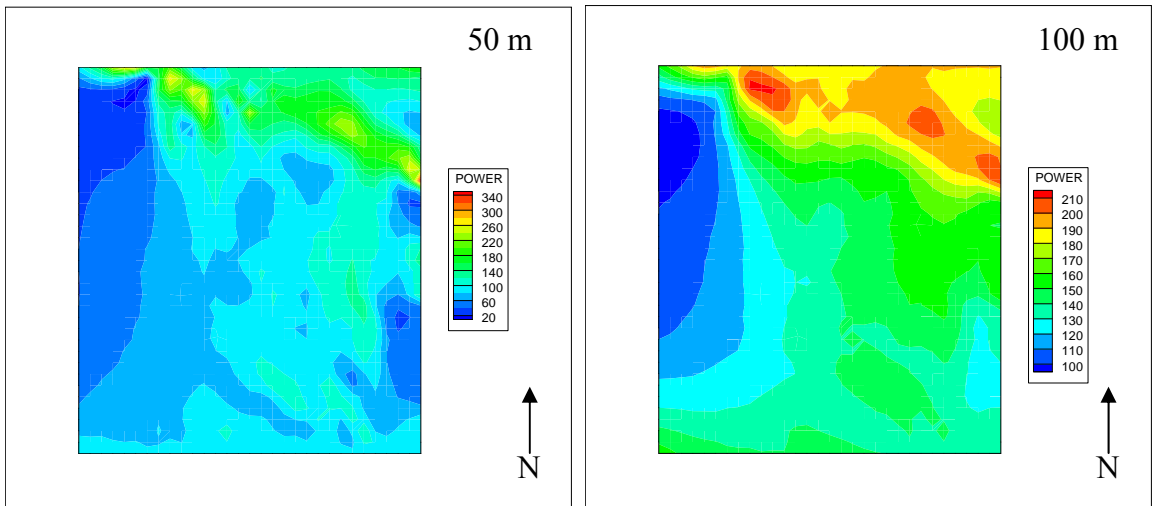
From the figure 4.8 it can be observed that the wind power density of the Nellis Dunes area at the 50 m and 100 m elevation is between 200 W/m$^2$ to 300 W/m$^2$.
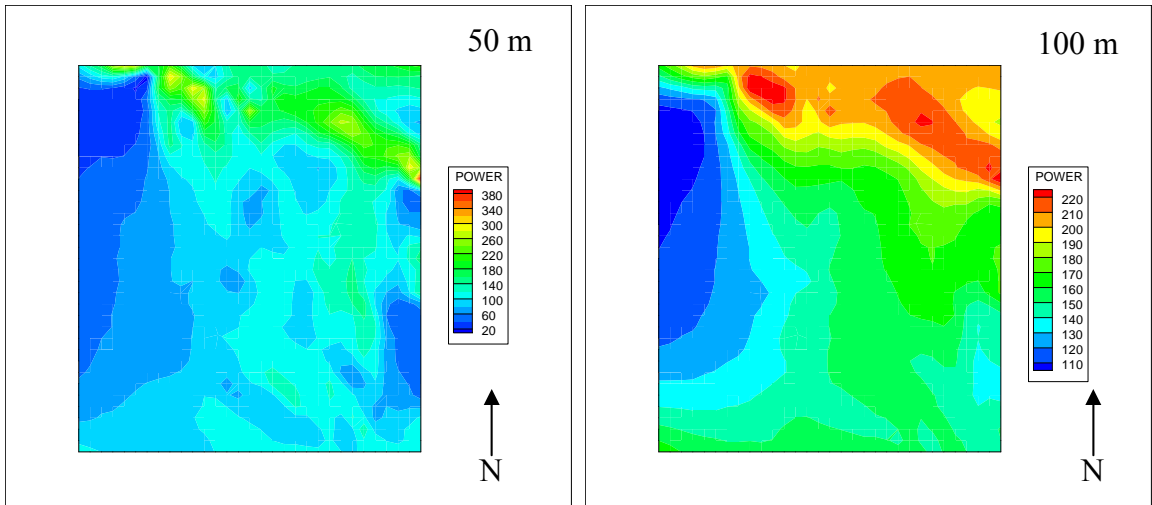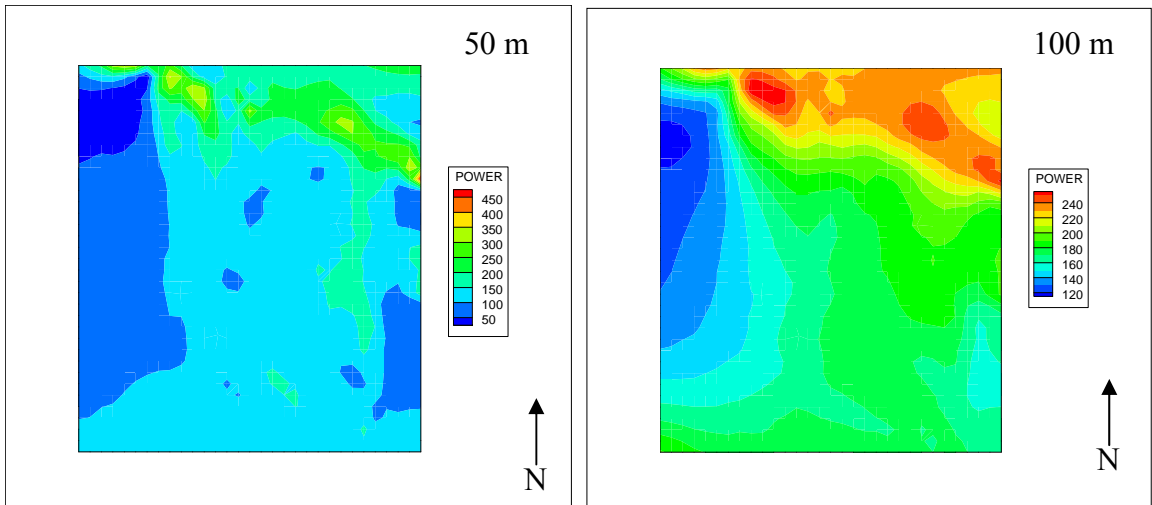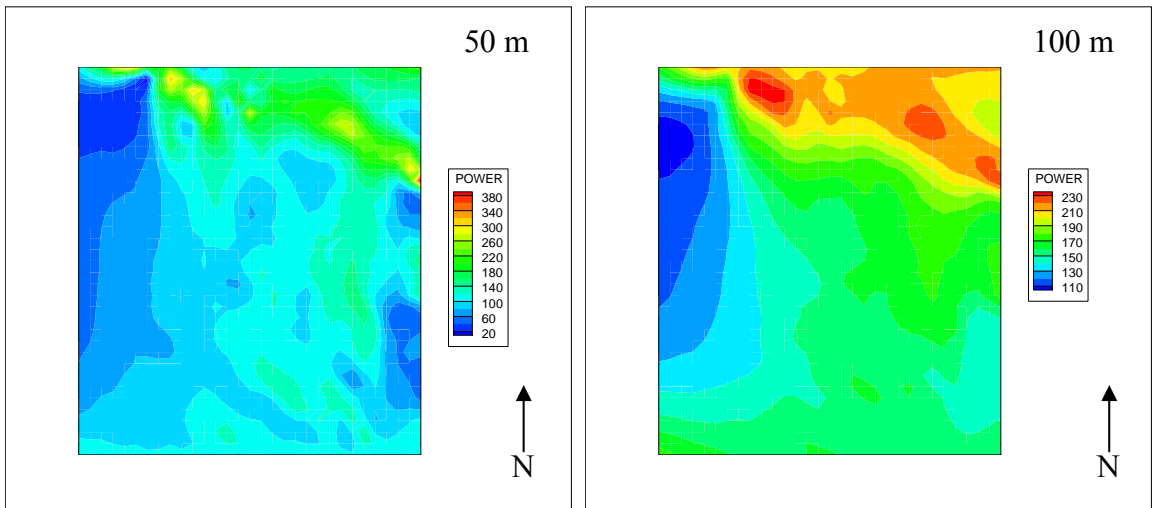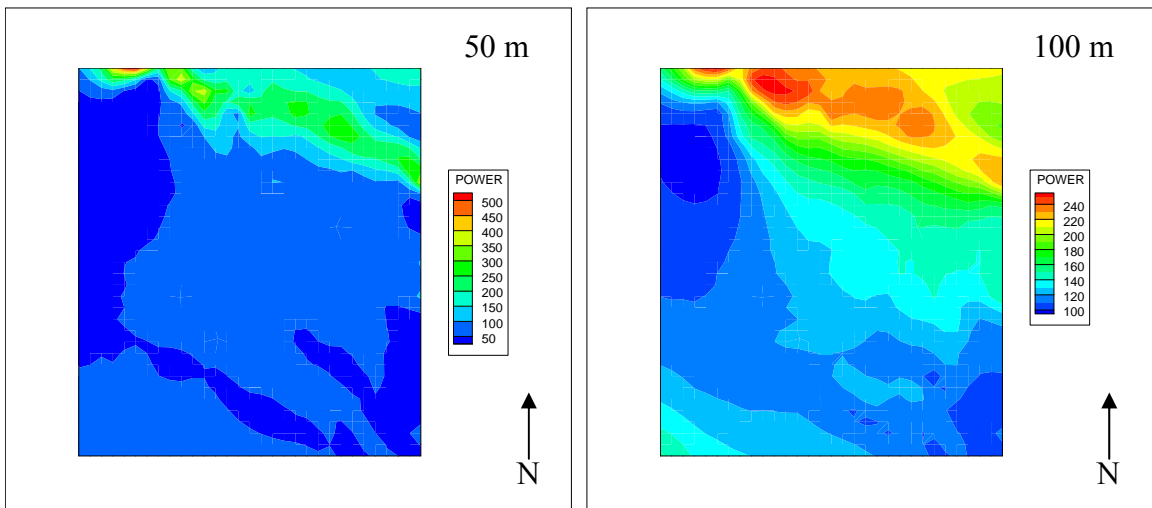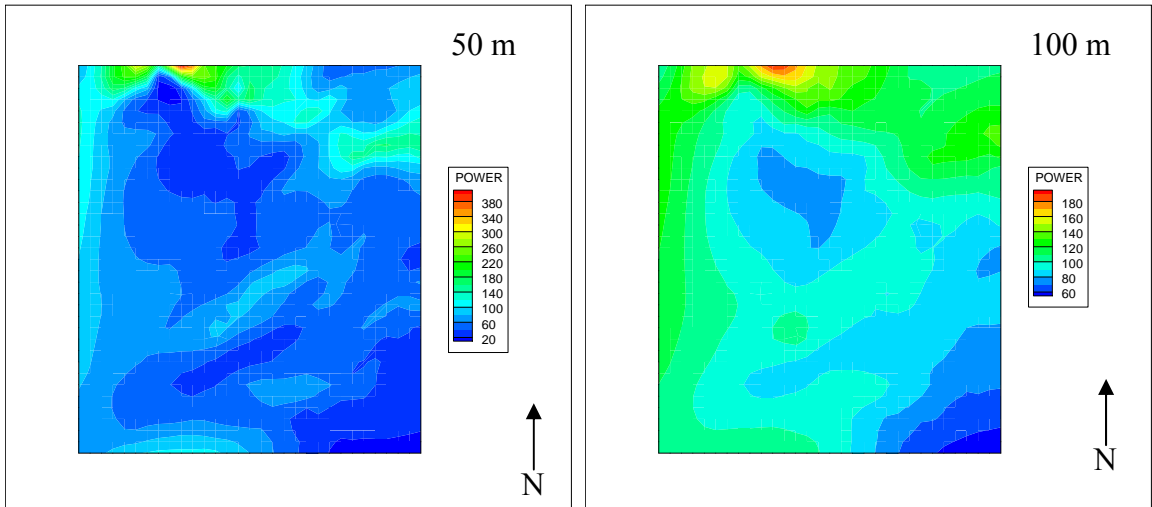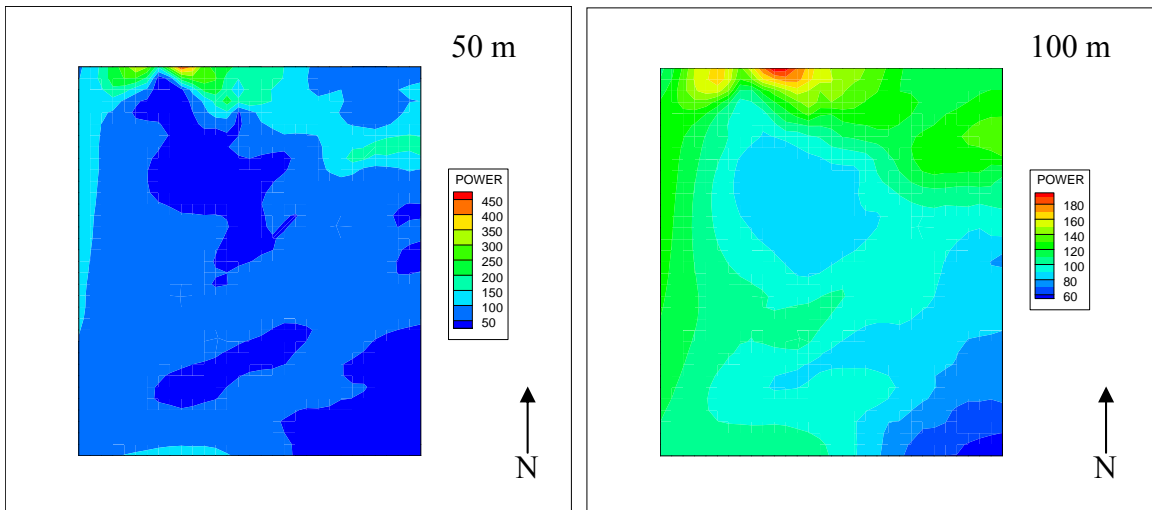
(a)  January
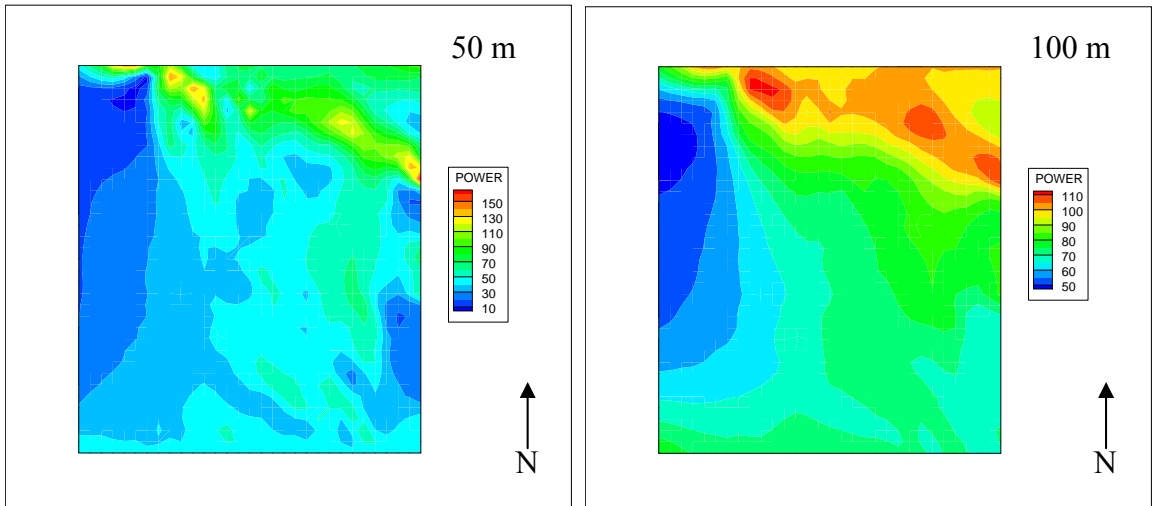


(b)  February



(c)  March
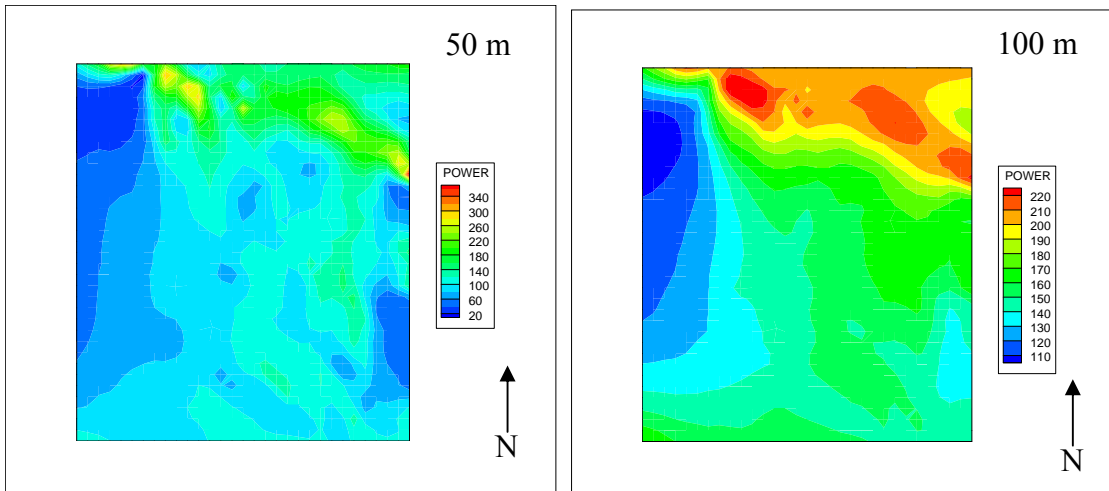
69

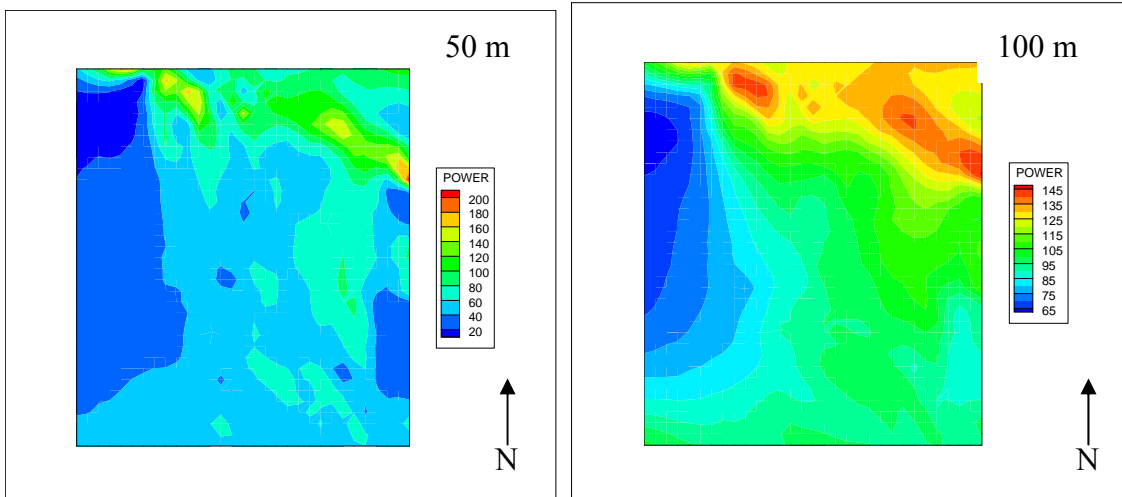(d) April



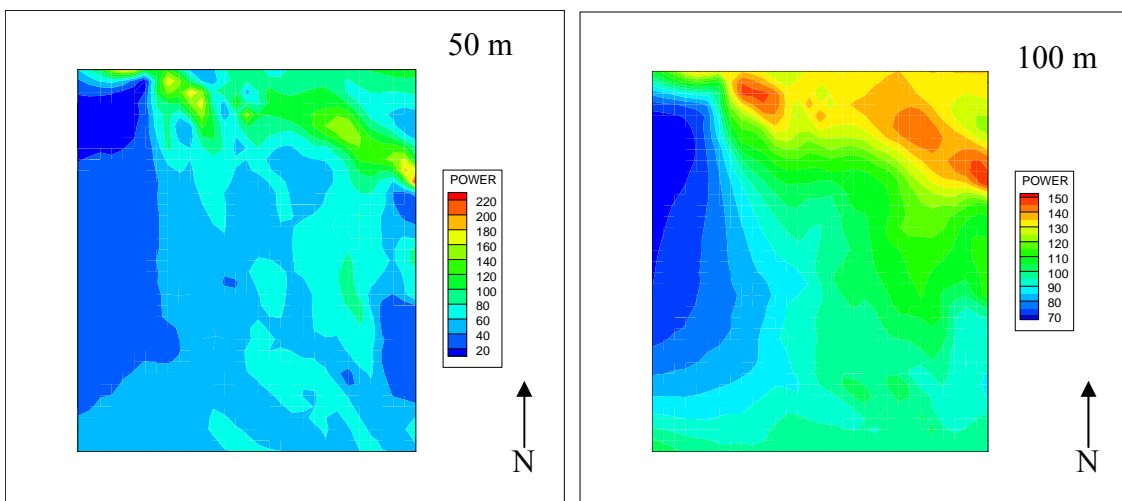(e) May



(f) June

70

(g)  July



(h)  August



(i)  Spetember

71

(j) October



(k) November



(l) December

Figure 4.8 Wind Power Density (WPD) plots

CHAPTER 5

CONCLUSIONS

Though the wind power densities for the whole of United States are available from other sources (TrueWind, etc.,) they give a mesoscale estimate of the wind power. A microscale estimation is more meaningful in finding the wind power potential of any site. Such studies have to be developed from local meteorological measurements taken over a period of at least a year.

In this study, a total of four meteorological towers were placed in the Nellis Dunes area for collecting data. Three of the towers were 20 m tall and one of the towers was 10 m tall. Wind Explorer (NRG Systems) was used to collect the monthly averaged wind data and the Symphonie Data Loggers (NRG Systems) were used to collect 10 min averaged data. Though data from Symphonie Data Loggers is much refined, data from Wind Explorer is sufficient enough to generate the monthly averaged wind field and also to carry out the statistical analysis of wind. In this study, wind speed at tower locations was smooth compared to other parts of the region. Placing the towers at locations where the wind speed has more variations can give much more accurate results. Increasing the number of towers will also increase the accuracy of the results. Also it is important to protect the towers from vandalism.

A 3-D wind field was constructed using meteorological data collected from meteorological towers. The finite element method is used to model the wind flow, since it allows the use of unstructured grids over any physical domain. DEM data was used to generate the ground level mesh and then the upper layers. Upper level wind fields were calculated using a surface boundary layer technique; vertical velocities were then

developed from the solutions of the continuity equation. An adjustment of the wind field is then obtained to ensure mass consistency. Mass consistent finite element method was used to generate the wind filed and it was found very efficient. By comparing the simulated results with the measured data for one of the towers, the goodness of the prediction of the windfield was also verified.

A statistical analysis of the measured monthly averaged wind data was also conducted. A good fit with the Weibull probability distribution was observed for three of the four tower values for the entire year. Wind rose diagrams for the entire year were also constructed to obtain monthly average wind directions.

Monthly averaged wind power densities were calculated for a period of one year for the Nellis Dunes Area in Nevada. The wind power for the selected region was determined to be between 200 W/m$^2$ to 300 W/m$^2$ with a wind power class of 2 to 3. Additional studies for the other regions of Nevada should be conducted, especially for those regions where the wind class is between 3 – 4.

Because of the unavailability of computer resources, adaptive techniques were not used in this study. Local mesh refinement can be obtained by the use of adaptation, which reduces the computer time by refining the mesh in the region where the velocity variations are more and making the mesh coarse at locations where the velocity is more uniform.

BIBLIOGRAPHY

AWS, Truewind

Dickerson, M. H., MASCON-A Mass Consistent Atmospheric Flux Model for Regions with Complex Terrain. J. Appl. Meteor.. 1978, 17, 241-253.

Goodin, W. R., Mcrae, G. J., Seinfeld, J. H. A Comparison of interpolation Methods for Sparse Data: Application to Wind and Concentration Fields. J. Appl. Meteor. 1979, 18, 761-771.

Kitada, T., Kaki, A., Ueda, H., Peters, L. K. Estimation of vertical air Motion from Limited Horizontal Wind Data-A Numerical Experiment. Atmos. Environ.. 1983, 17, 2181-2192.

Lange, R. A Three-Dimensional Transport-Diffusion Model for the Dispersal of Atmospheric Pollutants and its Validation Against Regional Tracer Studies. J. Appl. Meteor.. 1978, 17, 241-256.

Mathur, R., Peters, L. K. Adjustment of Wind Fields for Application in Air Pollution Modeling. Atmos. Environ.. 1990, 24, 1095-1106.

Montero, G., and Sanin, N. 3-D Modeling of Wind Field Adjustment Using Finite Differences in a Terrain Conformal Coordinate System. J. Wind Eng. Ind. Aerodyn.. 2001, 89, 471-488.

Patel, M. R. Wind and Solar Power Systems, Design, Analysis and Operation. Taylor and Francis Pub. 2006.

Pepper, D. W. A Finite Element Model for Calculating 3-D Wind Fields Over Vanderberg Air Force Base. 29th AIAA Aerospace Science Meeting, AIAA, 1991, Paper 91-0451, Reno, NV, American Institute of Aeronautics and Astronautics, 1-8.

Pepper. D. W., Brueckner, F. P. A Finite Element Model for Calculating 3-D Windfields over Irregular Terrain. 1992, FED-Vol. 143 / HTD-Vol.332.

Pepper, D. W., Heinrich, J. C. The Finite Element Method: Basic Concepts and Application. Taylor and Francis Pub: Washington, DC, 2006, 312 pp.

Pielke, R. Mesoscale Meteorological Modeling. Academic Press. 1984, 612 pp

Pielke, R. A., Mcnider, R. T., Segal, M., Mahrer, Y. Bull. Amer. Meteor. Soc.. 1983, 64, 243-249.

Ratto, C. F., Festa, R., Romeo, C., Frumento, O. A., and Galluzi, M. Mass-consistent Models for Windfields Over Complex Terrain: The State of the Art. Environ. Software, 1994, 9, 247-268.

Sasaki, Y. An Objective Analysis Based on the Variational Method. J. Meteor. Soc. Japan. 1958, 36, 77-88.

Schaefer, J. T., and Doswell III, C. A. On the Interpolation of a Vector Field. Mon. Wea. Rev., 1979, 107, 458-457.

Sherman, C. A. A Mass-Consistent Mode for Wind Fields over Complex Terrain. J. Appl. Meteor. 1978, 10, 377-386.

Warner, T. T., Anthes, R. A., Mcnab, A. L. J. Conf. Appl. Of Air Pollution Meteor.. Salt Lake City, Utah, Nov. 29-Dec. 2, 1977, 269-276.

Warner, T. T., Fizz, R. R., and Seaman, N. L. A Comparison of Two Types of Atmospheric Transport Models-Use of Observed Winds Versus Dynamically Predicted Winds. J. Climate Appl. Meteor., 1983, 22, 394-406.

Zienkiewicz, O. C., and Shu, R. J. Z. A Simple Error Estimator and Adaptive Procedure for Practical Engineering Analysis. Int. J. Numer. Methods Eng.. 1987, 24, 337-357.

VITA

Graduate College

University of Nevada, Las Vegas

Upendra Rangegowda

Degree:
Bachelor of Engineering, Mechanical Engineering, 2003
Visvesvaraya Technological University

Thesis Title: Wind Flow Modeling for Wind Energy Analysis of the Nellis Dunes Area in Nevada

Thesis Examination Committee:
Chairperson, Darrell Pepper, Ph. D.
Committee Member, William Culbreth, Ph.D.
Committee Member, Hui Zhao, Ph.D.
Graduate Faculty Representative, Laxmi Gewali, Ph.D.